

SPINS: A Structure Priors aided Inertial Navigation System

Yang Lyu * Thien-Minh Nguyen * Liu Liu[†] Muqing Cao* Shenghai Yuan*
Thien Hoang Nguyen * Lihua Xie*

Abstract

We propose a navigation system combining sensor-aided inertial navigation and prior-map-based localization to improve the stability and accuracy of robot localization in structure-rich environments. Specifically, we adopt point, line and plane features in the navigation system to enhance the feature richness in low texture environments and improve the localization reliability. We additionally integrate structure prior information of the environments to constrain the localization drifts and improve the accuracy. The prior information is called *structure priors* and parameterized as low-dimensional relative distances/angles between different geometric primitives. The localization is formulated as a graph-based optimization problem that contains sliding-window-based variables and factors, including IMU, heterogeneous features, and structure priors. A limited number of structure priors are selected based on the information gain to alleviate the computation burden. Finally, the proposed framework is extensively tested on synthetic data, public datasets, and, more importantly, on the real UAV flight data obtained from both indoor and outdoor inspection tasks. The results show that the proposed scheme can effectively improve the accuracy and robustness of localization for autonomous robots in civilian applications.

Keywords: Localization, SLAM, structure prior, UAV navigation, nonlinear optimization

1 Introduction

Autonomous vehicles, especially Unmanned Aerial Vehicles (UAVs), have attracted tremendous research interests in recent years due to their potential in improving efficiency and safety in many military and civilian applications (Cai et al., 2014). [One fundamental prerequisite for an autonomous vehicle to successfully execute missions is to accurately and reliably estimate its 6-DOF pose \(Zhang and Singh, 2015\), which requires delicate algorithm development and systematic integration. A detailed review of various localization systems is provided in \(Yuan et al., 2021\).](#) Due to physical and electromagnetic interferences, GPS systems may not provide persistent and reliable localization information in many complex environments, named as GPS-denied environments, making it a challenging task for a vehicle to carry out missions autonomously.

*Yang Lyu, Thien-Minh Nguyen, Muqing Cao, Shenghai Yuan, Thien Hoang Nguyen and Lihua Xie (corresponding author) are with School of Electrical and Electronic Engineering, Nanyang Technological University, 50 Nanyang Avenue, Singapore 639798.

[†]Liu Liu is with College of Engineering and Computer Science, Australian National University, Canberra ACT 0200, Australia.

There are mainly two approaches to handle the localization in a GPS-denied environment. The first approach is the simultaneous localization and mapping (SLAM) framework (Durrant-Whyte and Bailey, 2006), which is to incrementally track the local pose by estimating the relative transformation between two observation frames. The main drawback of a SLAM-based method is that the localization result drifts as time goes on due to the accumulated relative pose estimation errors (Strasdat et al., 2010). One may reason that causes the relative pose estimation error is that the salient point features, on which many localization methods are dependent, are insufficient in many challenging civilian environments. Line and plane features are considered as promising supplements to point features for robot localization, especially in many civilian environments. Line and plane features are considered as promising supplements to point features for robot localization. First, lines and planes are more structurally salient and therefore can be endowed with more prior information. Secondly, they are more stable than points with respect to lighting/texture changes. Finally, lines and planes are more ubiquitous in a structure rich environment, such as most infrastructures in urban cities. Thus, it is a good practice to additionally integrate line and plane features in the localization framework for many civil applications.

Another alternative is to localize the vehicle according to a prior map by matching the local observations to the map directly (Sattler et al., 2011). Although this method has no drift issue, it is not easy to apply this method solely to achieve reliable localization in many challenging environments. First, the prior-map-based localization requires a high-fidelity map that may not be available in many scenarios. Second, even if there is a prior map, the association between local observations and map information is usually sophisticated and time-consuming due to large differences in observation view angle, data resolution, and even data format (Sattler et al., 2018; Mühlfellner et al., 2016).

Reflecting on the pros and cons of the two distinct approaches, it is a good practice to combine them, namely, to lend some prior information of the map to aid the SLAM based navigation. A loosely coupled framework is proposed in (Platinsky et al., 2020), which incorporates global pose factors in the local SLAM optimization. The global pose is obtained by matching images with a global map. Article (Middelberg et al., 2014) uses a locally pre-stored 3D points cloud map to fix the drift of a local SLAM system in a tightly coupled framework. Similar works are also presented in (Zuo et al., 2020; Mur-Artal and Tardós, 2017) based on different sources of map. Although the combination methods above demonstrates improved localization performances, their frequent and indiscriminate map prior information integration may severely slow down the localization process. Therefore, it is important to determine what information to integrate into the SLAM process to make a balance between localization performance and efficiency.

Inspired by the discussions above, this paper proposes a Structure Priors aided Inertial Navigation System (SPINS) that combines SLAM-based and prior map-based localization method by lending feature level structure prior information to restrain the drift of the SLAM-based methods. To deal with the challenges such as feature deficiency, prior information association, and to achieve an efficient combination of the two methods in civilian environments with rich structure information, we make the following contributions:

To summarize, this paper makes the following contributions:

1. Firstly, we extend our previous work (Lyu et al., 2022) and further relief the feature deficiency problem by integrating 3D point, line, and plane features from various sensor modalities to relief the feature deficiency in civil environments. The heterogeneous features based localization is modeled in a sliding window fashion and solved with a graph optimization method.
2. With the heterogeneous feature used, we integrate more generic and broader range of prior information which we named as *structure priors* and parameterized as the relative distances/angles between different geometric primitives. The association between observation and map is therefore simplified to one dimension level. To ease the burden of integrating too many factors, we develop a structure prior information selection strategy based on the *information gain* to incorporate only the most effective structure priors for localization.
3. Finally, we test our proposed framework extensively based on synthetic data, public datasets, and real

UAV flight data obtained from both indoor and outdoor inspection tasks. The results indicate that the proposed framework can improve the localization robustness even in challenging environments.

The remainder of the paper is organized as follows. In Section 2, the related works are provided. The proposed SPINS framework is formulated in Section 3. The geometric features and structure priors are modeled in Section 4 and Section 5, respectively. Experiment validations are provided in Section 6. Section 7 concludes the paper.

2 Related works

SLAM-based localization is considered as one of the most promising approaches for robot localization. By measuring salient features from the environment, the robot can accumulatively estimate its pose in local coordinates, which is preferred in many challenging environments, such as complex indoor or urban cities (Weiss et al., 2011). In this part, we review the recent SLAM results based on different features and structure priors.

Among existing methods reported in the literature, the point feature is most commonly used in the environment perception front-end in SLAM frameworks, especially in the visual aided navigation frameworks. Some successful demonstrations, such as ORB-SLAM (Mur-Artal et al., 2015), and VINS-mono (Qin et al., 2018), utilize 2D point features from vision sensors to estimate the local motion and sparse 3D point clouds of the environment. With the development of more advanced 3D sensing technologies, navigation methods based on 3D sensors, such as stereo-vision (Lemaire et al., 2007), LiDAR (Zhang and Singh, 2014), and RGB-D camera (Sturm et al., 2012), can directly utilize 3D points with metric information in the estimation process, therefore can provide improved localization and reconstruction results. In addition to the most commonly used point features, line and plane features are also adopted as additional features in some mission scenarios, such as indoor servicing (Padhy et al., 2019; Lu and Song, 2015), structure inspection (Hasan et al., 2017; Nguyen et al., 2021a), and autonomous landing (Chavez et al., 2017), in case that point features are not sufficient.

In the past few years, SLAM methods using heterogeneous features have begun to draw researchers' attention. The improvement of localization performance has been verified by works with different feature combinations. In vision-based SLAM, line features are considered more effective than point features in a low textural but high structural environment with a proper definition of the state and re-projection error. Extended from the ORB-SLAM, the PL-SLAM (Pumarola et al., 2017) can simultaneously handle both point and line correspondences. The line state is parameterized with its endpoints, and the re-projection error is defined as point-to-plane distances between the projected endpoints of 3D line and the observed line on image plane. A tightly coupled Visual Inertial Odometry (VIO) exploiting both point and line features is proposed in (He et al., 2018). The line is parameterized as a six-parameter Plücker coordinate (Hodge et al., 1994) for transformation and projection simplicity, and a four-parameter orthonormal representation for optimization compactness. Similar reprojection error to (Pumarola et al., 2017) is utilized in (He et al., 2018; Lyu et al., 2022). Comparisons of different line feature parameterization are provided in (Yang et al., 2019) based on the MSCKF SLAM framework, which shows that the closest point (CP) based (Yang and Huang, 2019a) and quaternion based (Kottas and Roumeliotis, 2013) representations outperform the Plücker representation under noisy measurement conditions. Besides the monocular based methods above, a stereovision-based VIO using point and line features together is proposed in (Zheng et al., 2018) where the measurement model is directly extended from the monocular camera model similar to (Pumarola et al., 2017). In the stereo vision based PL-SLAM framework (Gomez-Ojeda et al., 2019), a visual odometry is formulated similarly to (Zheng et al., 2018). In addition to that, the key-frame selection and loop closure detection under point and line features setup are also provided.

As 3D sensors such as LiDAR or RGB-D camera become more popular, plane features now can be effectively extracted in a man-made environment. A Lidar Odometry and Mapping (LOAM) in real-time is proposed

in (Zhang and Singh, 2014), which utilizes plane features to improve the registration accuracy of a point cloud. A LiDAR-inertial SLAM framework based on 3D planes is proposed in (Geneva et al., 2018), where the closest point representation is utilized for parameterizing a plane. A tightly-coupled vision-aided inertial navigation framework combining point and plane features is proposed in (Yang et al., 2019), where a plane is parameterized similar to (Geneva et al., 2018). In addition, the point-on-plane constraint is incorporated to improve the VINS performance. Recently, point, line, and plane features are jointly applied in the SLAM frameworks (Zhang et al., 2019; Yang and Huang, 2019b; Li et al., 2020; Aloise et al., 2019) to realize stable localization and mapping in low texture environments. In (Zhang et al., 2019), the line and plane features are tracked simultaneously along a long distance to provide persistent measurements. Also, the relationship between features, such as co-planar points, is implemented to enforce structure awareness. Similar work (Li et al., 2020) utilizes line and plane to improve the feature richness and incorporates more spatial constraints to realize more robust visual inertial odometry. A pose-landmark graph optimization back-end is proposed in (Aloise et al., 2019) based on the three types of features, which are handled in a unified manner in (Nardi et al., 2019). A thorough theoretical analysis of implementing point, line, and plane features in VINS is provided in (Yang et al., 2019) where three kinds of features are parameterized as measurements to estimate the local state based on a recursive MSCKF framework. More importantly, the observability analysis of different combinations of features is provided, and the effect of degenerate motion is studied.

Although researchers have begun to introduce heterogeneous geometric features into their SLAM works, integrating prior map information to the localization still draws limited attention. There are mainly two types of prior information that can be obtained from a prior map to aid the SLAM, namely the global information and the local structure information. By incorporating global pose constraints by matching local observations with a consistent global map, the SLAM drift can be reduced. Inspiring by this, the global information is incorporated in the local SLAM in both loosely coupled manner (Platinsky et al., 2020) and tightly coupled manner (Middelberg et al., 2014).

On the other hand, only limited structure priors information, such as point-on-line, line-on-plane, and point-on-plane constraints, are considered in the SLAM. A visual inertial navigation system that utilize both point features and actively selected line features on image plane is proposed in (Lyu et al., 2022), structure prior information based on special point and line relationships are utilized to improve the localization performance. Note that the structure information is ubiquitous in civil environments that are rich of man-made objects. It is a practical wisdom to implement more general structure prior information of the environment to improve the localization and mapping quality rather than to consider the environment as entirely unknown. For instance, in a building inspection environment, the structure information, as elaborate as the CAD modes, or as coarse as some common sense such as flat planes, parallel lines, with proper parameterization, can be implemented to aid the localization process (Hasan et al., 2017; Jovančević et al., 2016).

3 System description

In this section, the SPINS is described from a systematic point of view. The functional blocks of the system are illustrated in Fig. 1. The SPINS depends on three types of information to fulfill the task of accurately and reliably localizing an autonomous vehicle in a challenging civilian environment, namely 1) ego-motion measurements from interoceptive sensors, such as the Inertial Measurement Unit (IMU), at high-frequency feeding streaming, and 2) detected/tracked point, line, and plane features from exteroceptive sensors, and 3) structure priors which are parameterized as pairwise high fidelity measurements between features.

3.1 Optimization formulation

The aforementioned three types of information within a sliding window are incorporated into a factor graph, which is a bipartite graph contains variables and factors. Specifically, the variables represent the state of the local vehicle and the heterogeneous features, and factors encode different types of observations and structure

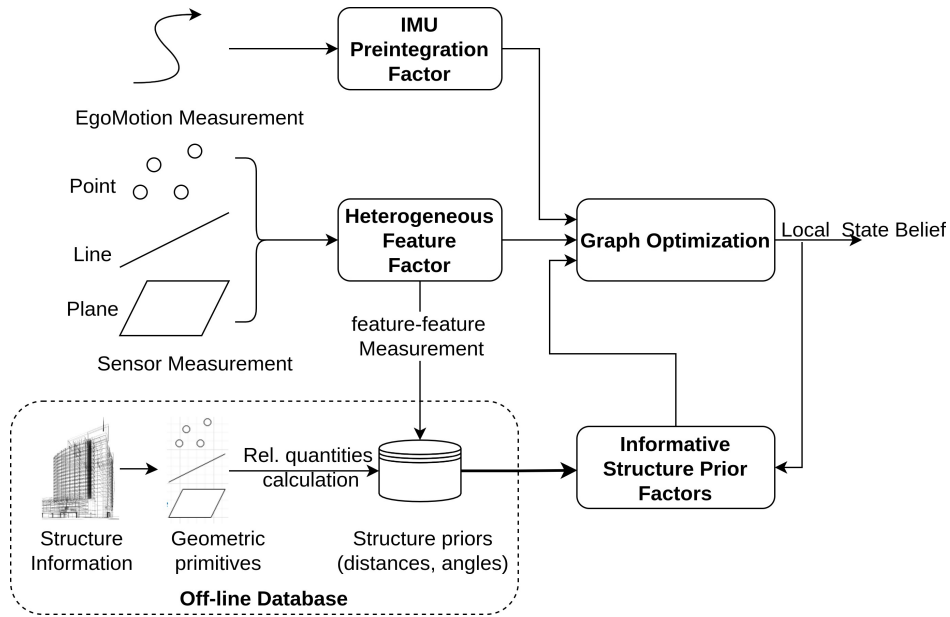
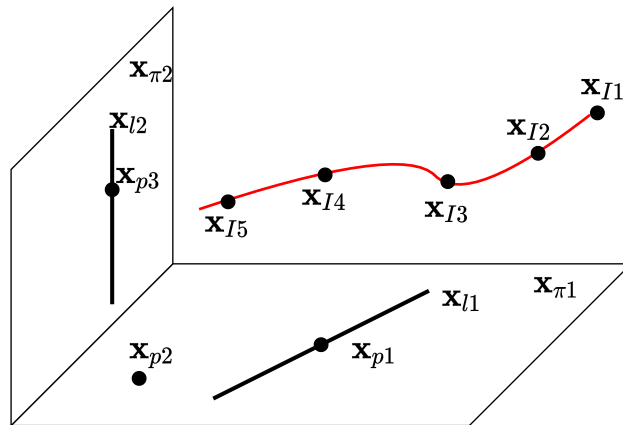
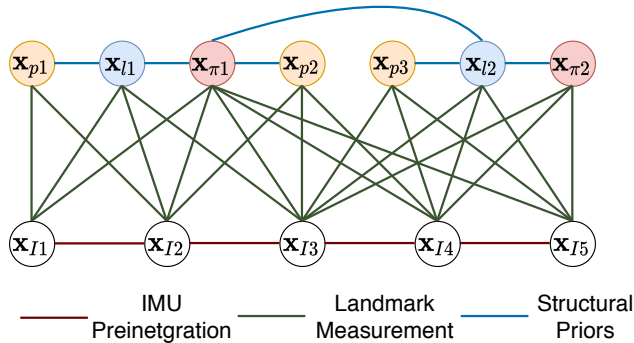


Figure 1: The systematic functional blocks of the proposed SPINS framework.



(a) A geometric representation of point, line and plane features.



(b) The corresponding factor graph of subfigure (a).

Figure 2: The factor graph including the structure priors.

priors. The states included in the sliding window at time t are defined as

$$\mathcal{X}_t \triangleq [\{\mathbf{x}_{I,m}^\top\}_{m \in T_t} \quad \{\mathbf{x}_i^\top\}_{i \in P_t} \quad \{\mathbf{x}_j^\top\}_{j \in L_t} \quad \{\mathbf{x}_k^\top\}_{k \in \Pi_t}]^\top, \quad (1)$$

where $\{\mathbf{x}_{I,m}\}_{m \in T_t}$ contains active IMU states within the sliding window at time instance t . T_t denotes the set of IMU measurements at t . P_t, L_t, Π_t denote the sets of point, line and plane features that are observed within the sliding window at time t , respectively. The IMU state is

$$\mathbf{x}_I \triangleq [{}^I_G \bar{q}^\top \quad {}^G \mathbf{p}_I^\top \quad {}^G \mathbf{v}_I^\top \quad \mathbf{b}_g^\top \quad \mathbf{b}_a^\top]^\top, \quad (2)$$

where ${}^I_G \bar{q}$ is a unit quaternion denoting the rotation from the global frame $\{G\}$ to the IMU frame $\{I\}$. ${}^G \mathbf{p}_I$ and ${}^G \mathbf{v}_I$ are the IMU position and velocity, respectively. $\mathbf{b}_g, \mathbf{b}_a$ are the random walk biases for gyroscope and accelerometer, respectively. With the state definition (1), the objective is to minimize the cost function of different measurement residuals in (3).

$$\begin{aligned} \min_{\mathcal{X}_t} & \left\{ \|\mathbf{r}_p\|_{\mathbf{P}_{p_t}}^2 + \sum_{m \in T_t} \|\mathbf{r}_{I,m}\|_{\Sigma_m}^2 \right. \\ & + \sum_{i \in P_t} \rho(\|\mathbf{r}_i\|_{\Sigma_i}^2) + \sum_{j \in L_t} \rho(\|\mathbf{r}_j\|_{\Sigma_j}^2) + \sum_{k \in \Pi_t} \rho(\|\mathbf{r}_k\|_{\Sigma_k}^2) \\ & \left. + \sum_{s \in \mathcal{S}_t} \rho(\|\mathbf{r}_s\|_{\Sigma_s}^2) \right\}. \end{aligned} \quad (3)$$

The first term of (3) is the cost on prior estimation residuals, and \mathbf{P}_{p_t} is the corresponding covariance prior to the optimization at t (Kaess et al., 2012). The second term is the cost of IMU-based residual, and $\mathbf{r}_{I,m}$ defines the measurement residual between active frames m and $m + 1$. The IMU measurement between time step m and $m + 1$ is obtained by integrating high-frequency raw IMU measurements continuously with the technique called IMU preintegration (Forster et al., 2017), and Σ_m is the corresponding measurement covariance. The second line of (3) represents the cost function of measurement residuals of point, line, and plane features and are weighted by their corresponding covariances. The third line is the cost of structure priors measurement residuals.

For a measurement in Euclidean space, its residual term is defined as the difference between the predicted measurement based on estimated state $\hat{\mathcal{X}}$ and a real measurement \mathbf{z} , as

$$\mathbf{r} = h(\hat{\mathcal{X}}) - \mathbf{z}, \quad (4)$$

where $h(\cdot)$ is the measurement prediction function for the estimated state between any two variables in the factor graph. The term $\|\mathbf{r}\|_{\Sigma}^2 = \mathbf{r}^\top \Sigma^{-1} \mathbf{r}$ is defined as the squared Mahalanobis distance with covariance matrix Σ . A huber loss $\rho(\cdot)$ (Huber, 1992) is applied on each squared term to reduce potential mismatches between states and measurements. The optimization of (3) is usually solved with an iterative Least-Squares solver through a linear approximation as detailed in Appendix A.

The formulation of measurement functions $h(\cdot)$ with regard to the geometric features and the structure priors are provided in 4 and Section 5, respectively.

3.2 Structure prior information

The structure information is ubiquitous, ranging from the fine-grained blueprint to common knowledge such as parallel lines or planes. The greatest challenge to integrate the prior information in the optimization is to correctly associate the structure information with the observed features. Benefiting from using point, line, and plane features simultaneously, we can parameterize the spatial relationship between different geometric features as pairwise relative distances and angles in Section 5. The advantages of using such parameterization are mainly three folds.

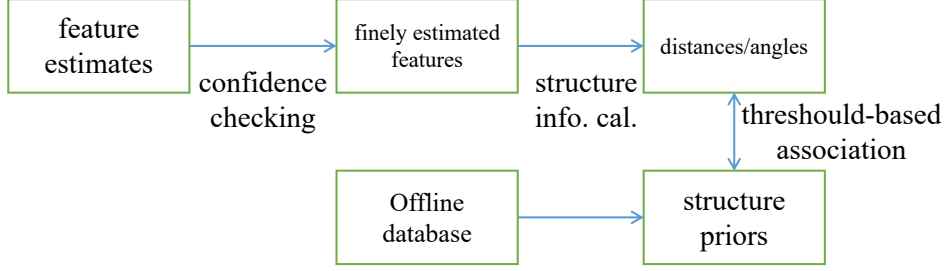


Figure 3: The online association between structure priors and local estimates.

1. First, the prior knowledge can be integrated in a simple fashion. With the distance and angle based formulation, the rigorous association process between the prior knowledge and current observation, which are normally based on high-dimensional and computational-demanding feature matching processes, can be simplified to a scalar level association based on thresholds.
2. Second, more extensive prior knowledge can be utilized to aid the navigation. The distances and angles can not only be extracted from prior maps with specific format, but also be obtained from structural common senses, hand-measured quantities, and so on.
3. As the angles and distances are stored as scalars, the storage can be reduced dramatically comparing to storing a map.

The structure priors can be extracted offline based on the following three steps:

1. extract structural primitives from various formats, *e.g.*, high fidelity maps, local measurements, semantic information *etc.* ,
2. measure and calculate the relative quantities between every two primitives (as formulated in Section 5), and
3. store salient structure quantities (distances/angles) as structure priors in a database.

The association process between offline structure prior information and online local observations is illustrated as Fig.3. Initially, finely estimated features within current optimization window are selected based on the estimation confidences. Then the structural quantities (angles/distances) based on the estimates can be calculated. Finally, a structure prior is integrated into the optimization when it is close enough to a structural quantity from estimates, based on a scalar threshold. Given two features' estimates, $\hat{\mathbf{x}}_i, \hat{\mathbf{x}}_j$, a distance/angle prior information z_s is associated to i, j when

$$|h_s(\hat{\mathbf{x}}_i, \hat{\mathbf{x}}_j) - z_s| \leq \tau_s,$$

where $h_s(\cdot)$ is the function to extract distance/angles (see Sec. V), and τ_s is a scalar threshold. To prevent possible false association of structure prior information, we set a very small threshold τ_s , and allow structure priors to be assigned to only finely estimated features.

Above structure priors integration process should be carried out based on following pre-requisites. First, the structure priors should be quantities that are identifiable among all relative distances and angles. Second, the structure prior quantity should be representative of the most salient structural patterns of an environment. In many robotic operation environment, such as indoor navigation, building inspection, geometric features are ubiquitous, and structure patterns are inerratic and repetitive. In such environment, the extracted structure priors (angles and distances) are sparsely distributed, see, *e.g.* Fig.8 and Fig.9, and the association can be achieved based on a simple threshold as described above. In this paper, we only consider structure rich environments where the sparseness of the structure priors holds.

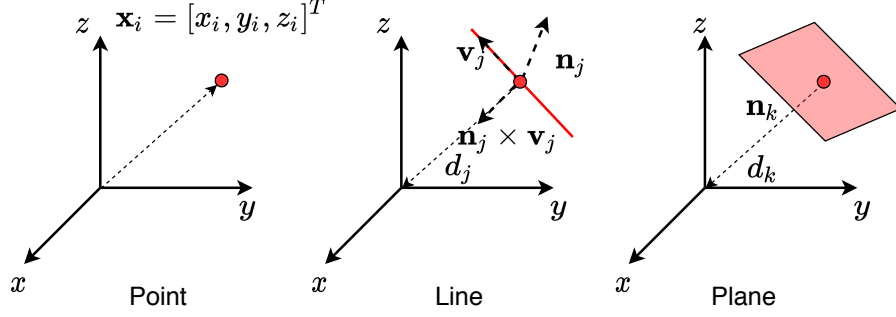


Figure 4: The geometry representation of point, line and plane in 3D space.

4 Heterogeneous geometric features

In this section, we discuss how to model the point, line, and plane features based on on-board perception and incorporate them into the graph optimization.

4.1 Point feature

As one of the most frequently implemented features in perception tasks, a point feature can be uniquely parameterized by its 3D coordinate, as shown in Fig. 4. A point feature $i \in P$ can be extracted from different sensors by measuring it in the local frame,

$$\mathbf{z}_i = h_i(\mathbf{x}_I, \mathbf{x}_i) + \boldsymbol{\nu}_i = {}^I_G \mathbf{R}({}^G \mathbf{p}_i - {}^G \mathbf{p}_I) + \boldsymbol{\nu}_i, \quad (5)$$

where ${}^G \mathbf{p}_i \in \mathbb{R}^3$ and ${}^G \mathbf{p}_I \in \mathbb{R}^3$ are the 3D positions of the point feature and the local vehicle in the global frame. $\boldsymbol{\nu}_i \in \mathbb{R}^3$ is the measurement noise. ${}^I_G \mathbf{R} \in \mathbb{SO}(3)$ represents the rotation from the local frame to the global frame. By defining the state of point feature as $\mathbf{x}_i = {}^G \mathbf{p}_i$, we have the Jacobians calculated in Appendix B.1.

4.2 Line feature

One most commonly implemented representation of a line feature in 3D space is its Plücker coordinates. For an infinite line $j \in L$, its Plücker coordinates are defined as $\mathbf{l}_j \triangleq [\mathbf{n}_j^\top \quad \mathbf{v}_j^\top]^\top$, \mathbf{n}_j and \mathbf{v}_j are the normal vector and directional vector calculated from any two distinct points on the line, as shown in Fig. 4.

A measurement of an infinite line can be modeled as its Plücker coordinates in the local frame as

$$\begin{aligned} \mathbf{z}_j &= h_j({}^G \mathbf{x}_I, {}^G \mathbf{l}_j) + \boldsymbol{\nu}_j \\ &= \begin{bmatrix} {}^I_G \mathbf{R} & -{}^I_G \mathbf{R} [{}^G \mathbf{p}_I]_\times \\ \mathbf{0}_3 & {}^I_G \mathbf{R} \end{bmatrix} {}^G \mathbf{l}_j + \boldsymbol{\nu}_j, \end{aligned} \quad (6)$$

where $\boldsymbol{\nu}_j \in \mathbb{R}^6$ is the measurement noise.

Obviously, the expression \mathbf{l}_j is not a minimum parameterization of the line state. To calculate the Jacobian, we implement the closest point approach described in (Yang and Huang, 2019b), which is formulated as $\mathbf{p}_j = d_j \bar{q}_j \in \mathbb{R}^4$, where the unit quaternion \bar{q}_j and the closest distance of the line to the origin can be

calculated from the Plücker coordinates respectively as

$$\mathbf{R}_j(\bar{q}_j) = \begin{bmatrix} \frac{\mathbf{n}_j}{\|\mathbf{n}_j\|} & \frac{\mathbf{v}_j}{\|\mathbf{v}_j\|} & \frac{\mathbf{n}_j}{\|\mathbf{n}_j\|} \times \frac{\mathbf{v}_j}{\|\mathbf{v}_j\|} \end{bmatrix}, \quad (7)$$

$$d_j = \frac{\|\mathbf{n}_j\|}{\|\mathbf{v}_j\|}, \quad (8)$$

where $\mathbf{R}_j(\bar{q}_j)$ is the corresponding rotation matrix to \bar{q}_j . By defining the line state as $\mathbf{x}_j = {}^G\mathbf{p}_j$, we have a minimum parameterization of the line in Euclidean space. The corresponding measurement Jacobians are provided in Appendix B.2.

4.3 Plane feature

An infinite plane $k \in \Pi$ can be minimally parameterized by the closest point $\mathbf{p}_k = d_k \mathbf{n}_k \in \mathbb{R}^3$, as shown in Fig. 4, where \mathbf{n}_k is the plane's unit normal vector, and d_k is the distance from the origin to the plane. The plane measurement here is modeled as the closest point in the local frame as

$$\mathbf{z}_k = {}^I\mathbf{p}_k + \boldsymbol{\nu}_k = {}^I\mathbf{n}_k {}^I d_k + \boldsymbol{\nu}_k, \quad (9)$$

where $\boldsymbol{\nu}_k \in \mathbb{R}^3$ represents the plane measurement noise. The translation of the unit normal vector and the distance of a plane from the global frame to the local frame is

$$\begin{bmatrix} {}^I\mathbf{n}_k \\ {}^I d_k \end{bmatrix} = \begin{bmatrix} {}^I_G\mathbf{R} & \mathbf{0}_{3 \times 1} \\ -{}^G\mathbf{p}_I^\top & 1 \end{bmatrix} \begin{bmatrix} {}^G\mathbf{n}_k \\ {}^G d_k \end{bmatrix}. \quad (10)$$

Incorporating (10) into (9), the plane measurement can be expressed with the normal vector ${}^G\mathbf{p}_I^\top$ and distance ${}^G d_k$ in the global frame as

$$\begin{aligned} \mathbf{z}_k &= {}^I d_k {}^I\mathbf{n}_k + \boldsymbol{\nu}_k = (-{}^G\mathbf{p}_I^\top {}^G\mathbf{n}_k + {}^G d_k) {}^I_G\mathbf{R} {}^G\mathbf{n}_k + \boldsymbol{\nu}_k \\ &= -{}^G\mathbf{n}_k^\top {}^G\mathbf{p}_I {}^I_G\mathbf{R} {}^G\mathbf{n}_k + {}^G d_k {}^I_G\mathbf{R} {}^G\mathbf{n}_k + \boldsymbol{\nu}_k. \end{aligned} \quad (11)$$

Define the state of a plane k as $\mathbf{x}_k = {}^G\mathbf{p}_k = {}^G d_k {}^G\mathbf{n}_k$, which is the closest point of the plane to the origin. we can calculate the measurement Jacobian in Appendix B.3.

Remark 1. *In our paper, the raw sensor measurement models of different geometric features are not explicitly provided since they are highly dependent on the sensing mechanism of different sensors. Our purpose here is to provide a common framework implementing the heterogeneous features rather than considering a specific sensor.*

5 Structure priors formulation

In this part, the structure priors are formulated as the relative relationships between features. Specifically, the angles and distances are defined between different geometric primitives, including point, line, and plane.

5.1 Feature-to-feature prior modeling

The structure prior factors are plotted as blue edges in the factor graph, as shown in Fig. ???. Denote the topology set containing all the pairwise structure priors as \mathcal{S} , then an edge $(a, b) \in \mathcal{S}$ indicates that some quantitative measurements between two features $a, b \in \{P, L, \Pi\}$, denoted as \mathbf{z}_{ab} , are known a priori. Let h_{ab} denote the measurement function between a and b , the structure prior residual can be obtained as

$$\mathbf{r}_{ab} = h_{ab}(\hat{\mathbf{x}}_a, \hat{\mathbf{x}}_b) - \mathbf{z}_{ab}. \quad (12)$$

The residual cost is

$$\sum_{(a,b) \in \mathcal{S}} \|\mathbf{r}_{ab}\|_{\Sigma_{ab}}^2, \quad (13)$$

where Σ_{ab} is the covariance of the measurement noise which represents the fidelity of implementing specific structure prior constraints. The covariance is assumed to follow Gaussian distribution and is calculated statistically during the structure priors extraction process. The following are to model the pairwise measurements between point, line, and plane features described above.

5.2 Feature-to-feature factors

5.2.1 Point-to-point factor

When two salient points are detected, the possible structure prior information that characterizes the spatial relationship can be modeled as a 1 – 3 dimensional measurement. Denote two point features $i, i' \in P$, and their relative translation $\mathbf{x}_{ii'} = \mathbf{x}_{i'} - \mathbf{x}_i$, the point-to-point structure measurement

$$\mathbf{z}_{ii'} = h_{ii'}(\mathbf{x}_{ii'}), \quad (14)$$

is to project the 3D displacement between the two points onto a specific 1-3 dimensional metric in the global frame. Specifically, the distance measurement can be modeled as $z_{ii'}^d = \|\mathbf{x}_{ii'}\|$.

The measurement residual Jacobians with respect to the points state are provided in Appendix C.1.

Remark 2. *In the point-to-point structure, the points should be salient in both texture and structure senses. In practice, most points are distributed according to the texture, and it may not be easy to endow structure information. Some examples of structurally salient points are intersection points, endpoints, and corner points. The integration of point-to-point structure prior information depends on the extraction and recognition of structural points, which may be challenging in practice.*

5.2.2 Point-to-line factor

The spatial relationship between a point and an infinite line can be described with a 2D vector. With a point $i \in P$ and a line $j \in L$, we define a 2D displacement between them as

$$\mathbf{x}_{ij} = \begin{bmatrix} \bar{\mathbf{n}}_j^\top \\ \bar{\mathbf{n}}_j^\top \times \bar{\mathbf{v}}_j^\top \end{bmatrix} \mathbf{x}_i + \begin{bmatrix} 0 \\ d_j \end{bmatrix} \in \mathbb{R}^2, \quad (15)$$

where $\bar{\mathbf{n}}_j = \frac{\mathbf{n}_j}{\|\mathbf{n}_j\|}$, $\bar{\mathbf{v}}_j = \frac{\mathbf{v}_j}{\|\mathbf{v}_j\|}$, and d_j are the line j 's unit normal vector, unit directional vector, and the distance to the origin point, respectively. Denote the point-to-line measurement of \mathbf{x}_{ij} as

$$\mathbf{z}_{ij} = h_{ij}(\mathbf{x}_{ij}), \quad (16)$$

The point to line distance can be calculated by letting $h_{ij}(\cdot)$ be a norm operator,

$$z_{ij}^d = d_{ij} = \|\mathbf{x}_{ij}\|. \quad (17)$$

Hereafter, the point-on-line constraint can be enforced as $d_{ij} = 0$. The measurement residual Jacobian is calculated as Appendix C.2.

5.2.3 Point-to-plane factor

The relationship between a point and an infinite plane can be described with one scalar, *i.e.*, the distance from the point to the plane. With a point feature $i \in P$, and an infinite plane feature $k \in \Pi$, the distance between a point and a plane is defined as

$$d_{ik} = (\mathbf{n}_k)^\top \mathbf{p}_i + d_k. \quad (18)$$

Define a measurement function as $z_{ik}^d = d_{ik}$, then the point-on-plane constraint can be enforced by letting $d_{ik} = 0$. The measurement residual Jacobian is provided in Appendix C.3.

5.2.4 Line-to-line factor

The relationship of two lines can be uniquely parameterized with a 3D translation vector and a rotation angle. Given two lines, denoted respectively as $j, j' \in L$, the rotation $\alpha_{jj'}$ and translation $\mathbf{d}_{jj'} \in \mathbb{R}^3$ can be calculated as follows:

$$\alpha_{jj'} = \mathbf{v}_j^\top \mathbf{v}_{j'}, \quad (19)$$

and

$$\mathbf{d}_{jj'} = \begin{cases} \mathbf{0}, & j \text{ and } j' \text{ intersection,} \\ \bar{\mathbf{d}}_{jj'}, & j \text{ and } j' \text{ are parallel,} \\ (\bar{\mathbf{v}}_j \times \bar{\mathbf{v}}_{j'})^\top \bar{\mathbf{d}}_{jj'} (\bar{\mathbf{v}}_j \times \bar{\mathbf{v}}_{j'}), & \text{otherwise,} \end{cases} \quad (20)$$

where $\bar{\mathbf{d}}_{jj'} = d_j \bar{\mathbf{n}}_j \times \bar{\mathbf{v}}_j - d_{j'} \bar{\mathbf{n}}_{j'} \times \bar{\mathbf{v}}_{j'}$. $d_j \bar{\mathbf{n}}_j \times \bar{\mathbf{v}}_j$ and $d_{j'} \bar{\mathbf{n}}_{j'} \times \bar{\mathbf{v}}_{j'}$ are the closest point of line j and j' to the origin. It is straightforward to prove that as the relative angle $\alpha_{jj'} \rightarrow \pm 1$, the distances $d_{jj'} = \|\mathbf{d}_{jj'}\|$ denotes the relative distance between two parallel lines.

We first consider the rotation $\alpha_{jj'}$ as a measurement between two lines. Further, when two lines are parallel, namely $\alpha_{jj'} = \pm 1$, the distance $d_{jj'} = \|\mathbf{d}_{jj'}\|$ is considered as another measurement, namely

$$\mathbf{z}_{jj'} = \begin{cases} [\alpha_{jj'} & d_{jj'}]^\top, & \text{in parallel,} \\ \alpha_{jj'}, & \text{otherwise.} \end{cases} \quad (21)$$

The Jacobian of line-line measurement residual is provided in C.4.

5.2.5 Line-to-plane factor

The spatial relationship between a line and a plane can be characterized by the dot product of the directional vector of a line $j \in L$ and the normal vector of a plane $k \in \Pi$, denoted as α_{jk} :

$$\alpha_{jk} = \bar{\mathbf{v}}_j^\top \mathbf{n}_k. \quad (22)$$

Especially, when $\alpha_{jk} = 0$, namely a line is parallel to a plane, a distance can be further calculated as

$$d_{jk} = \mathbf{n}_k^\top (\bar{\mathbf{n}}_j \times \bar{\mathbf{v}}_j) d_j - d_k. \quad (23)$$

The measurement therefore is

$$\mathbf{z}_{jk} = \begin{cases} [\alpha_{jk} & d_{jk}]^\top, & \text{in parallel,} \\ \alpha_{jk}, & \text{otherwise.} \end{cases} \quad (24)$$

Specifically, the line-on-plane constraint is enforced as $\alpha_{jk} = 0$, and $d_{jk} = 0$. The associated Jacobian is provided in Appendix C.5.

5.2.6 Plane-to-plane factor

Similar to the above formulations, a similar dot product between the unit normal vectors of two planes, can be calculated as

$$\alpha_{kk'} = \mathbf{n}_k^\top \mathbf{n}_{k'}. \quad (25)$$

When two planes are parallel, the displacement can be calculated based on the closest points of two planes as

$$\mathbf{d}_{kk'} = \mathbf{x}_{k'} - \mathbf{x}_k = \mathbf{n}_k (d_{k'} - d_k) = \mathbf{n}_{k'} (d_{k'} - d_k). \quad (26)$$

Table 1: The structure priors formulated as distances/angles

	Point i	Line j	Plane k
i	$d_{ii'}$	d_{ij} e.g. point-on-line: $d_{ij} = 0$	d_{ik} e.g. point-on-plane: $d_{ik} = 0$
j	—	$\alpha_{jj'}$ $d_{jj'}$ if parallel e.g. orthogonality: $\alpha_{ij} = \pm 0$	α_{jk} d_{jk} if parallel ($\alpha_{jk} = 0$) e.g. line-on-plane: $d_{jk} = 0, \alpha_{jk} = 0$ orthogonality: $\alpha_{jk} = \pm 1$
k	—	—	$\alpha_{kk'}$ $d_{kk'}$ if parallel $\alpha_{kk'} = \pm 1$ e.g. orthogonality: $\alpha_{kk'} = \pm 1$

Define the measurement of the relationship as

$$\mathbf{z}_{jk} = \begin{cases} [\alpha_{kk'} & d_{kk'}]^T, & k \text{ parallel to } k', \\ \alpha_{kk'}, & \text{otherwise.} \end{cases} \quad (27)$$

The measurement Jacobians are provided in Appendix C.6. With the above formulation of spatial relationships between features, the structure priors can be encoded into low dimensional angles and/or distances, as summarized in Tab 1. The low dimensional encoding makes their associations with the structure priors database easy. Both the heterogeneous geometric feature factors and the structure prior factors are further integrated with the graph optimization toolbox GTSAM (Dellaert, 2012).

5.3 Structure prior selection

Based on the above formulations of the structure information between features, there are at most $n(n-1)/2$ possible feature priors in a scenario with n geometric features. In the graph optimization process, incorporating too many structure priors will severely damage the sparsity of the graph matrix, therefore will slow down the optimization. As an illustrative example, a synthetic environment with 100 points, 40 lines, and 40 planes are shown in Fig. 5. Despite the localization error decreases as more structure priors are incorporated into the optimization, the optimization efficiency deteriorates simultaneously. Among all the potential prior information, some are not as helpful as others, and there may also exist redundancies in the structure priors set.

Based on above observations, it is a practical trick to select a limited number of structure prior measurements which benefit the localization the most. Specifically, we consider to minimize the localization uncertainty represented by a estimation covariance. In this paper, we consider implementing the Fisher Information Matrix (FIM) to measure the contribution of a structure prior to the localization performance. Denote the belief of the state within the sliding window of time t as $\mathcal{X}_t \sim \mathcal{N}(\bar{\mathcal{X}}_t, \mathbf{P}_t)$, and one structure prior $s \in \mathcal{S}$ of current local map as a measurement, $h_s(\mathcal{X}_t) \sim \mathcal{N}(\mathbf{z}_s, \Sigma_s)$, we have the following equation according to the Bayes' rule

$$\mathbf{P}_{t+}^{-1} = \mathbf{P}_t^{-1} + \sum_{s \in \mathcal{S}_t} \mathbf{I}_s, \quad (28)$$

where $\mathbf{I}_s = \mathbf{J}_s^T \Sigma_s^{-1} \mathbf{J}_s$ is the FIM of a specific structure prior s . \mathbf{J}_s is the Jacobian of the structure prior s with regard to the local pose. \mathbf{P}_t and \mathbf{P}_{t+} denote the covariance before and after integrating the structure priors, respectively.

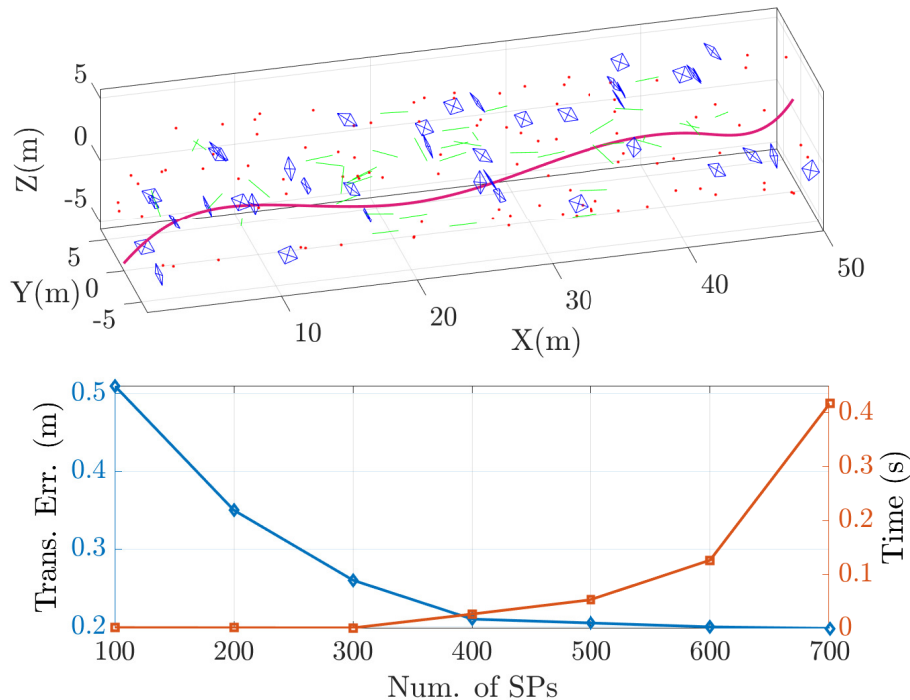


Figure 5: The translational estimation error and calculation time as number of SP grows.

Finally, we can use the marginalization technique (Carlone and Karaman, 2019) to obtain the localization uncertainty \mathbf{P}'_t by marginalizing out other states. The structure priors can be selected by minimizing a metric of the covariance \mathbf{P}'_t . The selection problem is NP-hard and cannot be solved efficiently for a large number of structure priors. As indicated in (Shamaiah et al., 2010), the $\log \det(\cdot)$ metric of the covariance is submodular w.r.t. the information gain of structure priors. With efficient greedy algorithms, a sub-optimal solution with guaranteed performance can be obtained more efficiently. We use selection algorithm similar to (Lyu et al., 2022) to obtain the structure prior set.

6 Experiment evaluation

In this part, the proposed SPINS is tested based on synthetic data, the public datasets, and, most importantly, on real flight datasets that are collected with a UAV during indoor and outdoor inspection tasks.

6.1 Synthetic data

To evaluate the localization performance of the proposed framework, we create a customized 2.5D indoor simulation scenario with point, line, and plane features as presented in Fig. 6. A 3D robot trajectory is generated within the simulation space based on spline functions as a red curve. An IMU is simulated according to the ADIS16448 IMU sensor specifications listed in (Geneva et al., 2018). We assume that the 3D geometry information of the features is obtained according to the measurement function described in Section 4 with extra FOV limitations.

The optimization-based localization is solved with the iSAM2 solver from the GTSAM packag, which we

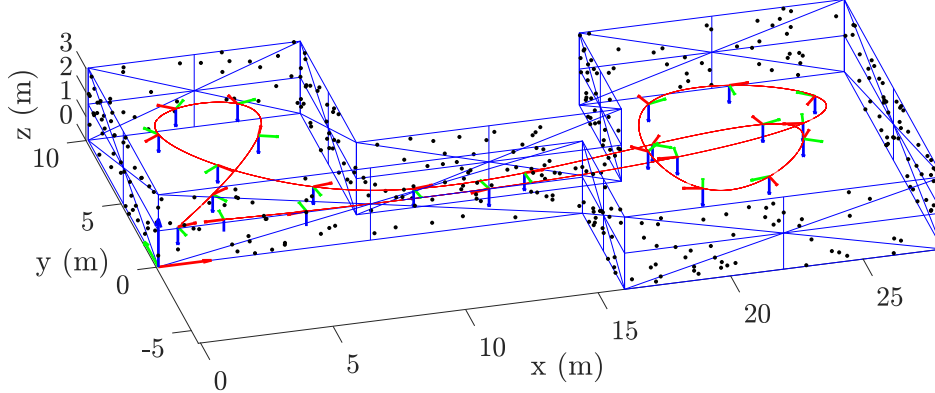


Figure 6: The 2.5D simulation scenario with point, line and plane features.

Table 2: Structure Priors between Features.

	Line	Plane
Point	Points on the Line	Points on the Plane
Line	-Parallelism with distance -Orthogonality	-Orthogonality -Parallelism with distance -Line on the Plane
Plane	-	-Parallelism with distance -Orthogonality

additionally integrate line factors, plane factors, and structure prior factors. Comparisons based on different features and structure prior factors are carried out. Specifically, we consider 1) point feature (P-INS), 2) point and line features (PL-INS), 3) point, line, and plane features (PLP-INS) based methods, and 4) our structure prior aided method (SPINS). We select 1) 20 structure priors in each frame randomly (SPINS-Rand. 20 SP), 2) 20 structure priors according to Section 5.3 (SPINS-App. Info. Opt. 20 SP), 3) the most informative 20 structure priors (SPINS-Info. Opt. 20 SP), and 4) all structure priors (SPINS-All SP). The structures information listed as Table 2 are adopted. In addition, a prior map based localization method is used as a localization benchmark where perfect feature matching between local observations and map is assumed.

The root-mean-square errors (RMSEs) are plotted in Fig. 7. The quantitative comparison between different strategies is also provided in Tab. 2. The localization results of using heterogeneous features are plotted as solid lines in different colors. It is apparent that, as more types of feature are used, more accurate estimation can be achieved. More important, the integration of structure prior information can further improve the localization performance, as plotted in dashed lines. Specifically, integrating all structure prior information unsurprisingly achieves the closest localization performance to the prior map based method. Nevertheless, the computation time for solving each round of the local optimization also significantly increases due to more structure factors are integrated, as provided in Tab. 2. Among the 20 structure priors based method, the optimal selection achieves the best performance, at the expense of greedy search computation overhead. Our proposed method achieved comparable result but with much less computation burden. Random selection based localization result is the least accurate.

6.2 Euroc dataset

In this part, the proposed SPINS framework is tested on the public Euroc MAV Dataset (Burri et al., 2016). The front-end detection and track point, line and planes based on stereo vision measurements. Specifically, the point features are detected and tracked with the KLT based optical flow method similar to (Qin et al.,

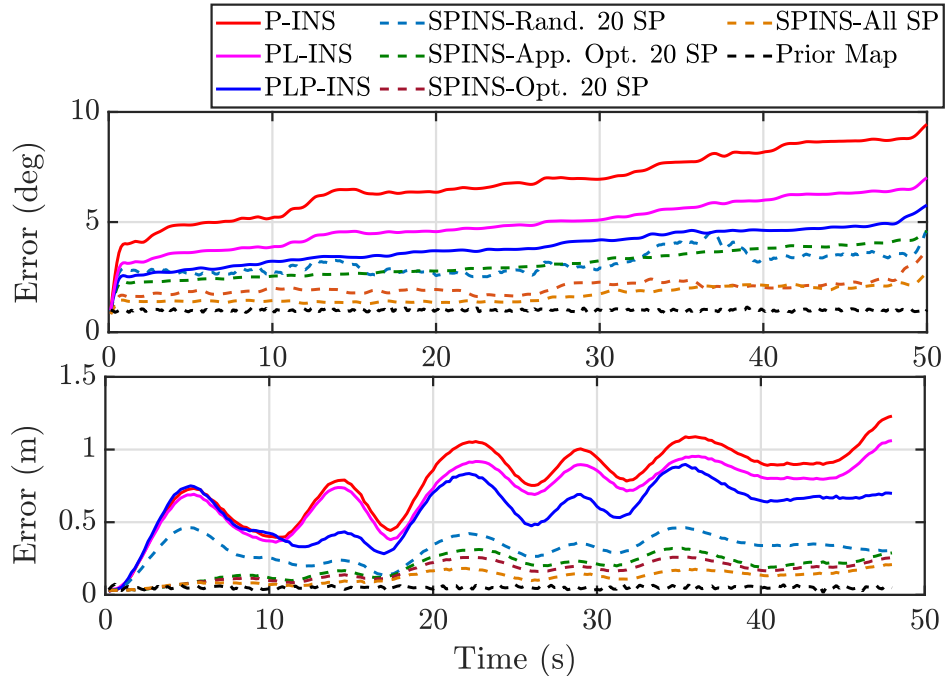


Figure 7: The translational and rotational RMSE under different feature and prior information configurations.

Table 3: Average RMSE over 100 Mento-Carlo simulations with different strategies.

Strategies	Trans. Errors [m]	Rot. Errors [deg.]	Time per iteration [s]
P-INS	0.8186	6.9399	0.0180
PL-INS	0.6103	5.0499	0.0193
PLP-INS	0.4863	3.9595	0.0274
SPINS-Rand. 20 SPs	0.3242	3.1684	0.0259
SPINS-App. Opt. 20 SPs	0.2082	3.1652	0.0301
SPINS-Opt. 20 SPs	0.1757	2.0399	0.3175
SPINS-All SPs	0.1277	1.6984	0.2463
Prior Map	0.0547	0.9414	—

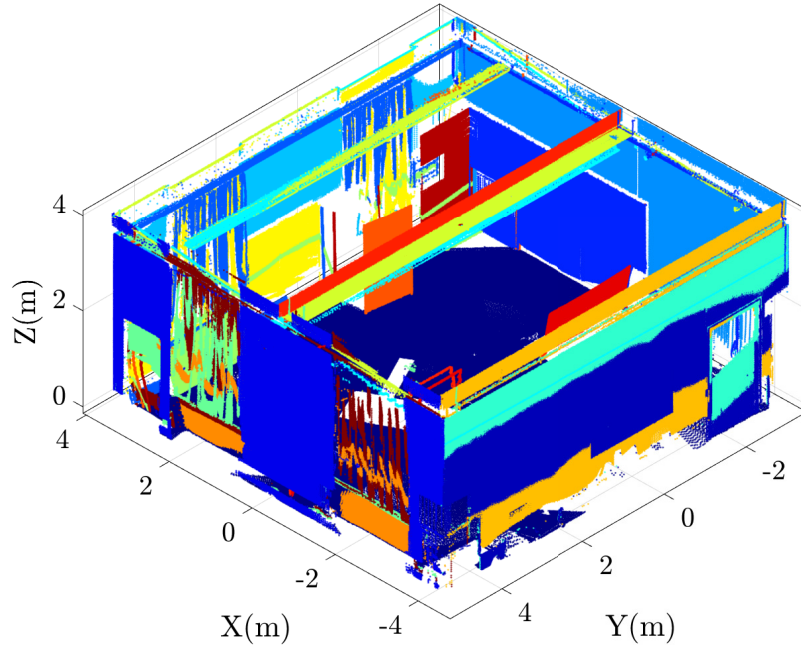


Figure 8: The structure priors extracted from the ground-truth scan of the vicon room.

2018). The line features are detected and tracked based on a modified line segment detector (LSD) as described in (Fu et al., 2020). Moreover, the planes are extracted and tracked based on triangulated point features based on the method described in (Nardi et al., 2019).

On the prior information part, we use the point cloud from the Vicon room to obtain the plane related structure priors. The plane extraction based on the point cloud is shown in Fig. 8. The corresponding distributions of angles between planes and the distances of parallel planes are plotted in Fig. 9, which show the repetition and sparsity angle and distance pattern in a man-made environment. Based on the prior information above, we extract the distance priors, such as point-on-plane, line-on-plane, and plane-to-plane distances, and angles priors, such as plane parallel, plane orthogonality, as structure priors to aid the localization.

The localization results by implementing the VINS FUSION(<https://github.com/HKUST-Aerial-Robotics/VINS-Fusion.git>), ORB-SLAM3 (https://github.com/UZ-SLAMLab/ORB_SLAM3.git), the heterogeneous features based method(Yang and Huang, 2019b), and the proposed framework are listed in Table 4 based on the evaluation method described in (Zhang and Scaramuzza, 2018). We use the same experiment setup for all tests according to the Euroc dataset parameters. As indicated, our proposed method can achieve the best performance in both translational and rotational RMSE in V1_01, V2_01, V2_02 and V2_03. Specifically, our proposed SPINS outperforms the PLP based method(Yang and Huang, 2019b) in all datasets, which shows the effectiveness of incorporating structure prior information.

As one example, the results of estimated trajectories of v2_02 are plotted in Fig. 10.

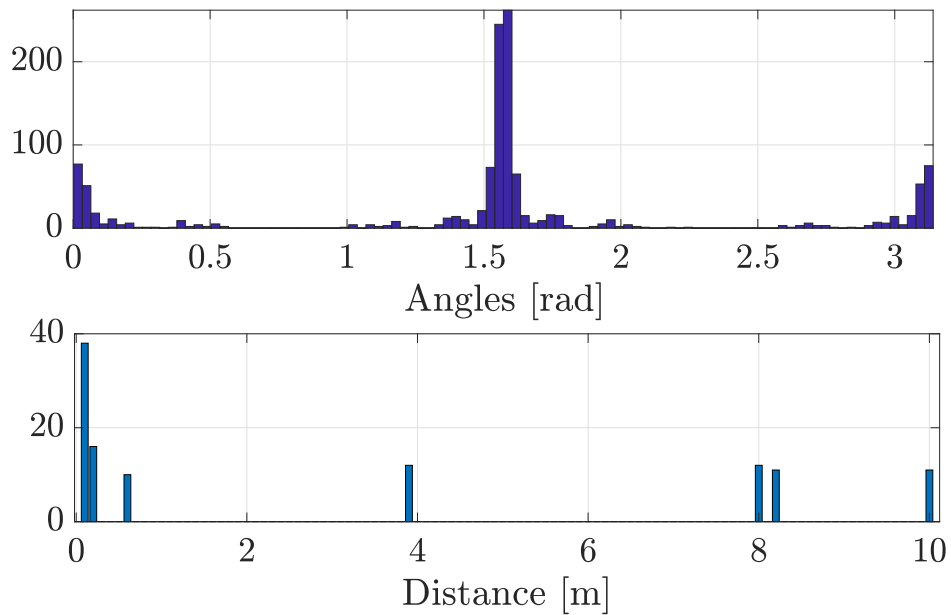


Figure 9: The angles and distances distribution of segmented planes in Fig.8

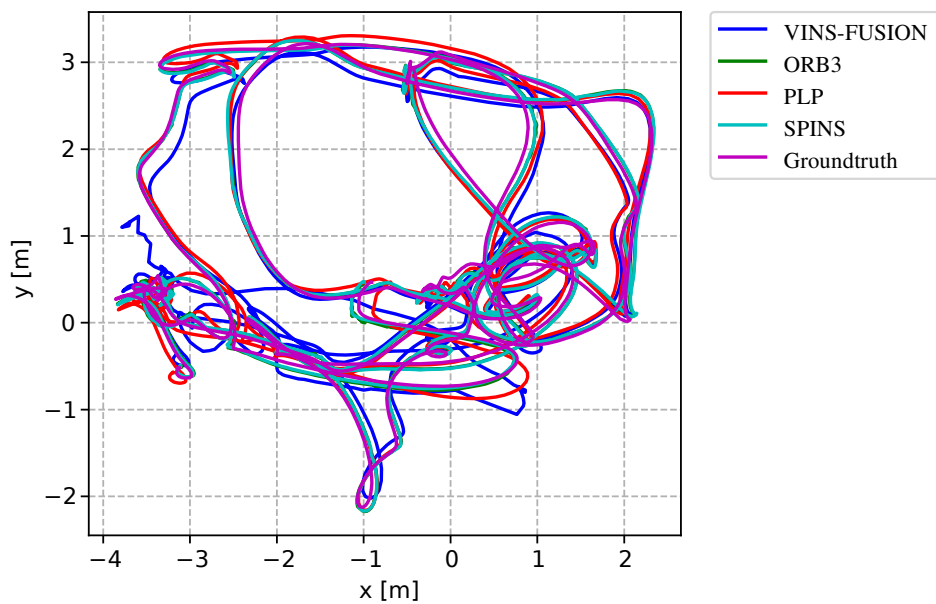


Figure 10: The estimated trajectories of V1.03 based on the VINS-FUSION, ORB3 and the proposed SPINS with PLP and PLP-SP setups.

Table 4: The RMSE of the estimation results based on different methods

Data	Trans. RMSE [m]/Rot. RMSE [°]			
	VINS	ORB3	PLP	SPINS
V1_01	0.129/1.748	0.085/1.484	0.098/1.674	0.079/1.131
V1_02	0.145/1.504	0.089/1.336	0.321/1.455	0.094/ 0.905
V1_03	0.144/1.967	0.093/1.952	0.193/2.389	0.095/ 1.762
V2_01	0.150/3.121	0.085/1.852	0.116/2.352	0.077/1.731
V2_02	0.197/4.413	0.167/3.141	0.188/4.581	0.160/3.030
V2_03	0.219/2.924	0.160/3.007	0.213/3.458	0.151/2.988

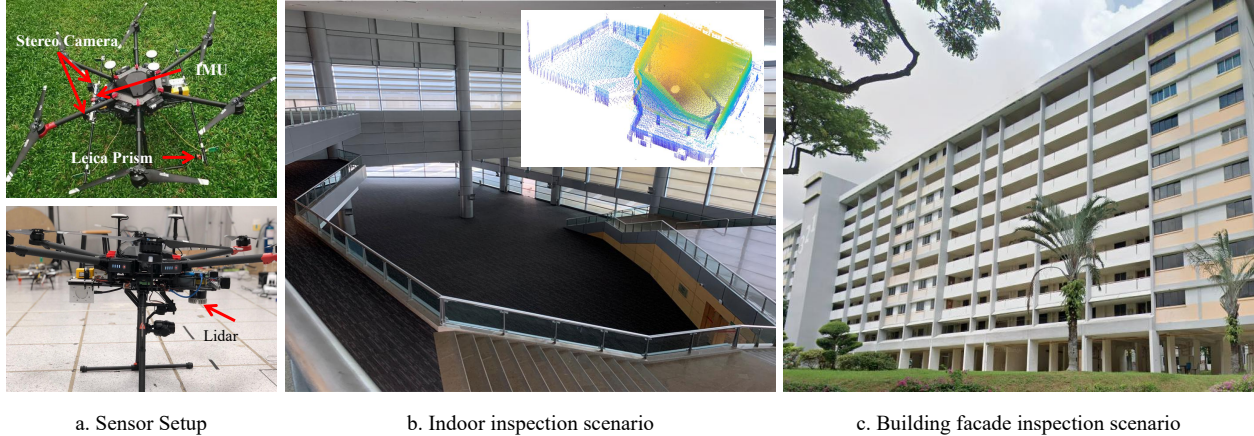


Figure 11: The experiment setups. We test the SPINS in both indoor (b) and outdoor (c) inspection scenarios.

6.3 Field collected data

In this part, the proposed SPINS is further tested on large scale inspection environment. A DJI M600 pro hexacopter carrying various sensors is utilized to detect features of the environment, as illustrated in Fig.11(a). We considered two scenarios where geometric feature and structure patterns are rich, as shown in Fig.11(b) indoor navigation and Fig.11(c) building façade inspection, which is available as part of the VIRAL dataset(Nguyen et al., 2021b).

We collect sensing data from visual cameras, LiDARs, and IMU sensors to properly detect the geometric features based on similar front-end processing to Sec. VII.B. The ground truth is provided by a Leica Geosystem that measures the optical prism onboard. All tests are carried out based on the same parameter setup provided in https://ntu-ariss.github.io/ntu_viral_dataset/.

6.3.1 Indoor navigation

In this part, the proposed structure prior information is further tested on an indoor auditorium. Similarly, we measure some potentially repetitive and salient features as the structure prior information. Moreover, we use the Leica system to obtain a point cloud map to extract plane based structure priors similar to Sec. VII.B. Three different trajectories are generated to test the proposed methods.

We compare our results to methods based on monocular camera (VINS-Mono (Qin et al., 2018)), stereo-camera (VINS-Stereo (Qin et al., 2019)), Lidar (LOAM (Zhang and Singh, 2014)), Lidar and Camera (LVI-SAM (Shan et al., 2021)), a map based localization method (DLL (Caballero and Merino, 2021)), and our method (SPINS). The ICP method by registering Lidar scans to point cloud map is also provided as a

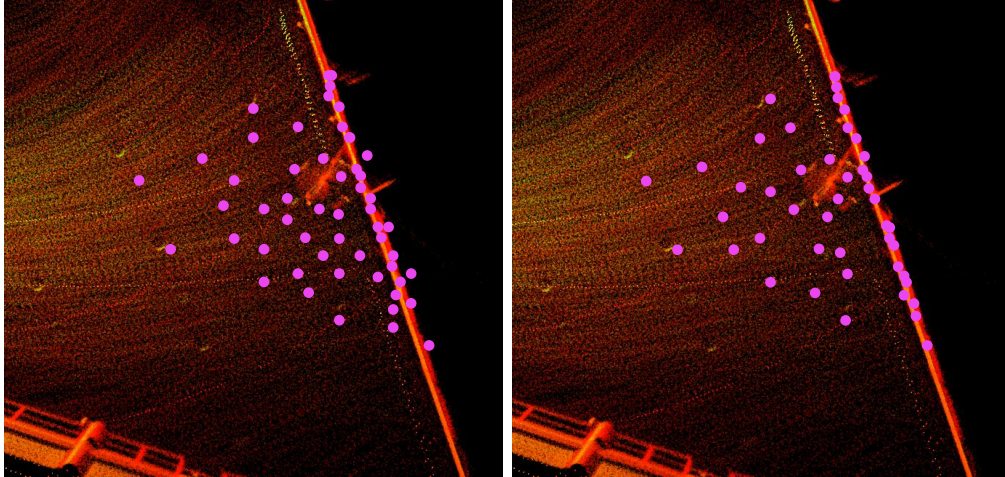


Figure 12: The point feature estimation before/after integrate the point-on-line constraint. When the constraint is imposed, the points on the wall are more accurately stick to the wall, lead to better point feature estimation.

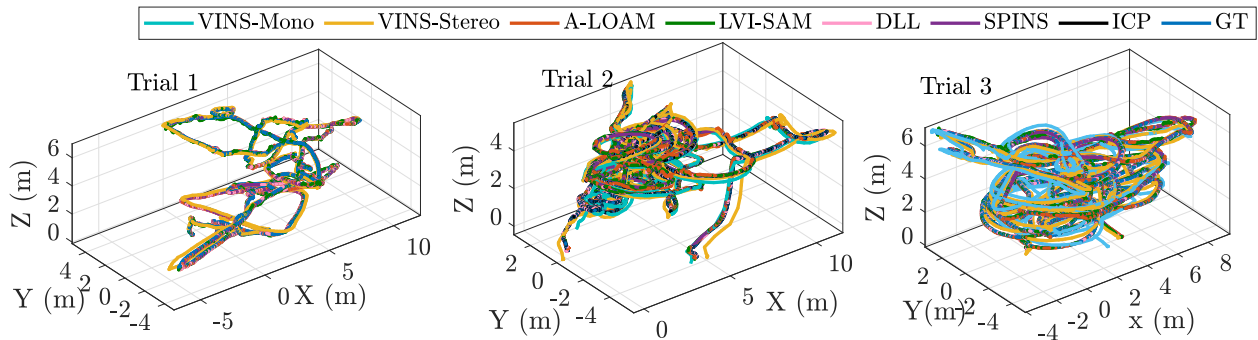


Figure 13: The estimated trajectories based on different methods.

localization benchmark. More specifically, we use the LOAM odometry for ICP and DLL initialization. The parameters are set as 50 iterations and 0.05m max correspondence distance in ICP. The estimated trajectories of 3 trials based on the above methods are plotted in Fig.13. The estimation errors of NYA03 is given in Fig. 14. The position RMSE based on the methods are provided in TABLE 5. It's apparent, our proposed method, aided by the angle/distance priors (as plotted in Fig. 15), can achieve the best performance among methods mentioned above. Moreover, the distances structure priors are more favored in most cases comparing to angles priors. One example of the effectiveness by imposing point-on-plane constraint, or zero point-to-plane distance constraints, is shown in Fig. 12.

Additionally, we compare our method to the prior map based method DLL. Although the DLL method can achieve very close performance to the SPINS in both accuracy and time efficiency, it requires an odometry to provide the initialization for registration between map and local scan, which is an extra computation burden. In addition, the DLL method requires an initial position of the robot in the map, which may not be available in practical scenarios. The ICP based method is also provided to indicate the best localization performance that map-based method can achieve. However, the ICP method uses more than 2 seconds for each registration process, and is hard to be implemented in real time applications.

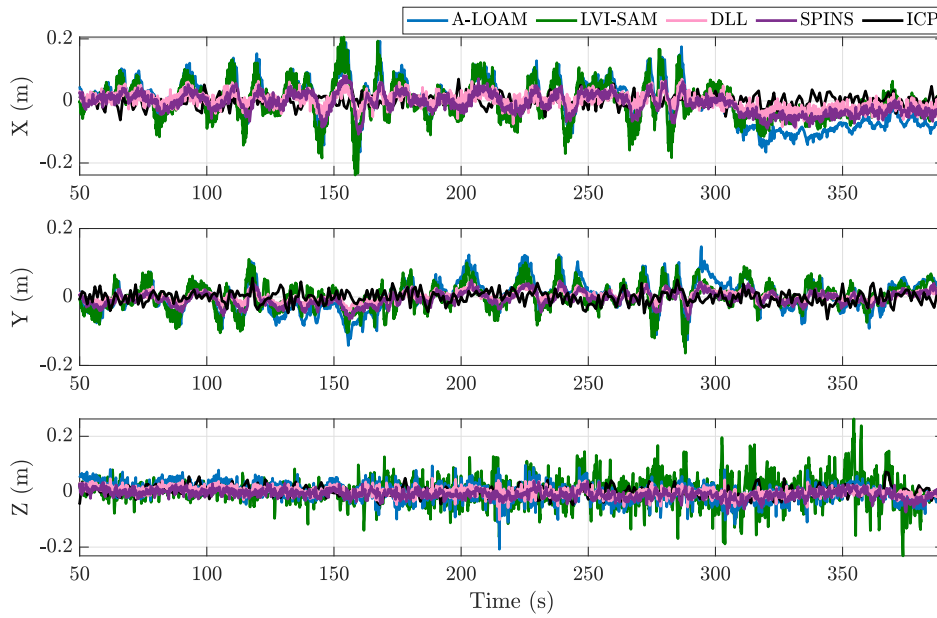


Figure 14: The estimation errors of different methods.

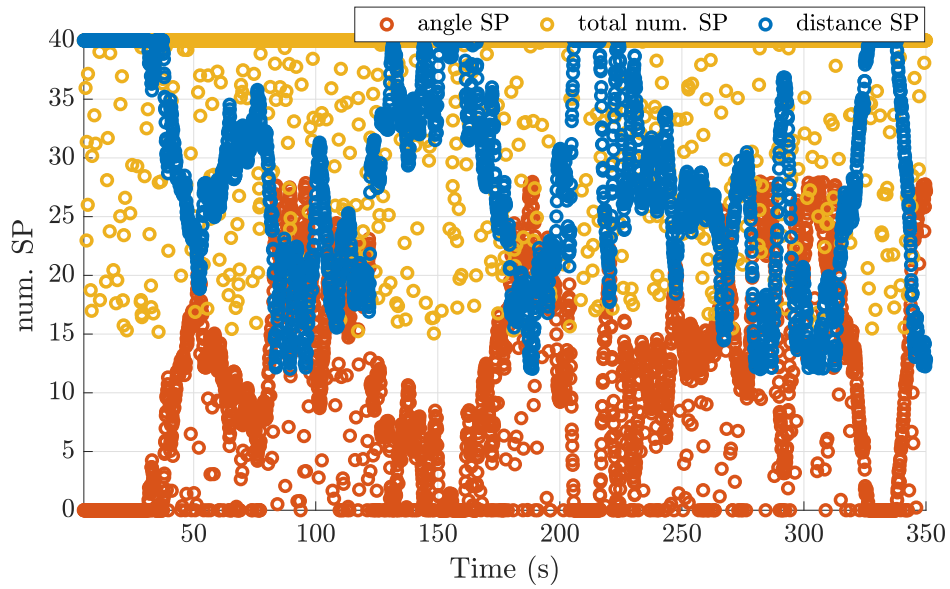


Figure 15: The number of angle and distance structure priors

Table 5: The RMSE of the estimation results based on different methods

Methods	Translational RMSE [m]			Time per iteration [s]
	NYA01	NYA02	NYA03	
Vins-Mono	—	0.2576	0.6118	—
Vins-Stereo	0.2427	0.2424	0.3808	—
ALOAM	0.0768	0.0902	0.0797	—
LVI-SAM	0.0761	0.0885	0.0827	—
DLL	0.0734	0.0663	0.0607	0.0911
SPINS	0.0551	0.0672	0.0592	0.0798
ICP	0.0262	0.0253	0.0214	2.003

Table 6: Hand-measured distances for the building

Distance Type	Typical Value [m]
Parallel Lines	[0.3, 0.5, 1.2, 1.5, 2.5, 3.3, 4]
Parallel Line to Plane	[0.5, 1.2, 2.7, 3, 4]
Parallel Planes	[1.5, 3, 4.5, 6]

6.3.2 Building inspection

In the larger scale building inspection task, the UAV is driven to follow a trajectory covering the façade of the building. The geometric feature extraction is shown in Fig. 16. To utilize our proposed SPINS method, we manually measure some distances and angles, which we treated as main patterns of the building, are summarized as Table 6.

The localization results of the inspection using different methods are presented from Fig. 17 to Fig. 19. A demonstrative video is provided at https://youtu.be/p-wca_WekvQ. The trajectories of different localization methods along with the ground truth (GT) are plotted in Fig. 17, although all trajectories are initialized at the same $[0, 0, 0]^T$, the trajectories from the VINS drifts as time goes on. Specifically, from Fig. 18, it’s clear that the trajectories from VINS drifts in x and y directions due to the low feature density and variation during the horizontal movement, and on the other hand, the trajectory from A-LOAM drifts mainly in the z direction due to low depth variation during vertical movement in z direction movement in a 2.5D building. As indicated in Fig. 19, the results obtained by using point, line and plane features apparently have better performance in all three directions. Moreover, the integration of structure priors SPINS outperformed the PLP method with the provide structure prior information. The position estimation RMSE of the

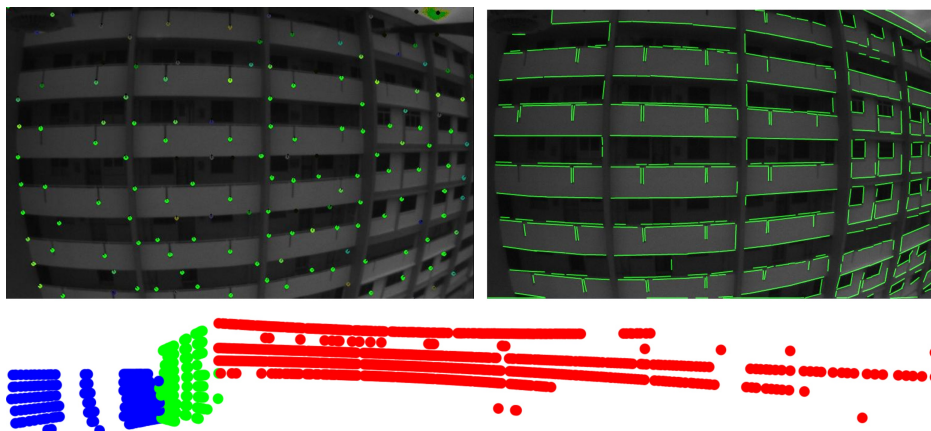


Figure 16: The extraction of point, line and plane features from both vision and LiDAR.

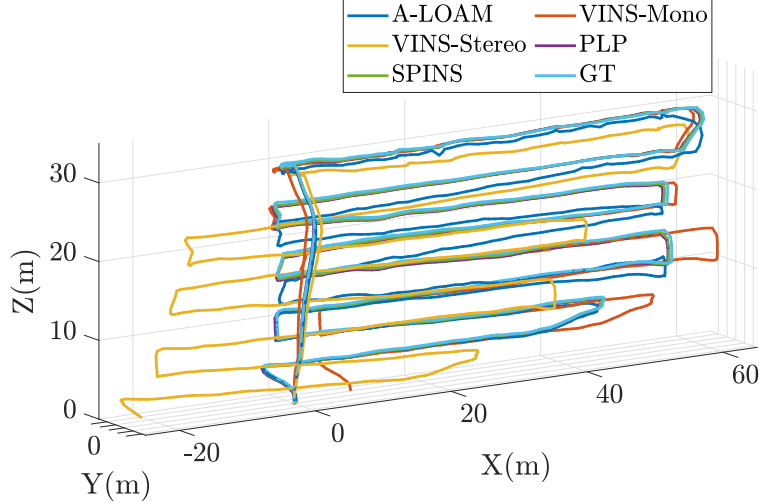


Figure 17: The estimated trajectories from different methods.

PLP and SPINS are 1.018m and 0.7452m, respectively, with a significant position accuracy improvement by incorporating the structure priors.

7 Conclusions

We propose a sliding window optimization-based localization framework utilizing point, line, and plane features. Considering heterogeneous features, we further develop a structure priors integration method that can further improve localization robustness and accuracy. To alleviate the computation burden brought by extra structure factor edges in the factor graph, we adopt a screening mechanism to select the most informative structure priors. Although the proposed SPINS shows advantages in civilian environments in our experiment, its effectiveness in more generic environments is questionable. In the future, we will further investigate on using general semantic prior information to aid the localization to achieve more wide range of environment adaptation.

A Least-Square solver

In the non-Euclidean space \mathcal{X} , the approximation is achieved by expanding the residual around the origin of a chart computed at current estimation $\hat{\mathcal{X}}$ as

$$\begin{aligned} \mathbf{r}(\hat{\mathcal{X}} \boxplus \Delta\mathcal{X}) &\approx \mathbf{r}(\hat{\mathcal{X}}) + \frac{\partial \mathbf{r}(\hat{\mathcal{X}} \boxplus \Delta\mathcal{X})}{\partial \Delta\mathcal{X}} \Big|_{\Delta\mathcal{X}=\mathbf{0}} \Delta\mathcal{X} \\ &= \mathbf{r}(\hat{\mathcal{X}}) + \mathbf{J}\Delta\mathcal{X}. \end{aligned} \quad (29)$$

The operator \boxplus applies a perturbation $\Delta\mathcal{X}$ to the manifold space \mathcal{X} . Specifically, for the Euclidean states, the \boxplus operator degenerates to the vector addition operator. \mathbf{J} is the sparse Jacobian matrix with only none zero block on the related two states. Incorporating the approximation (29) into (3), we have the following form

$$\Delta\mathcal{X}^T \mathbf{H} \Delta\mathcal{X} + 2\mathbf{b}^T \Delta\mathcal{X}^T + \text{const}(\hat{\mathcal{X}}), \quad (30)$$

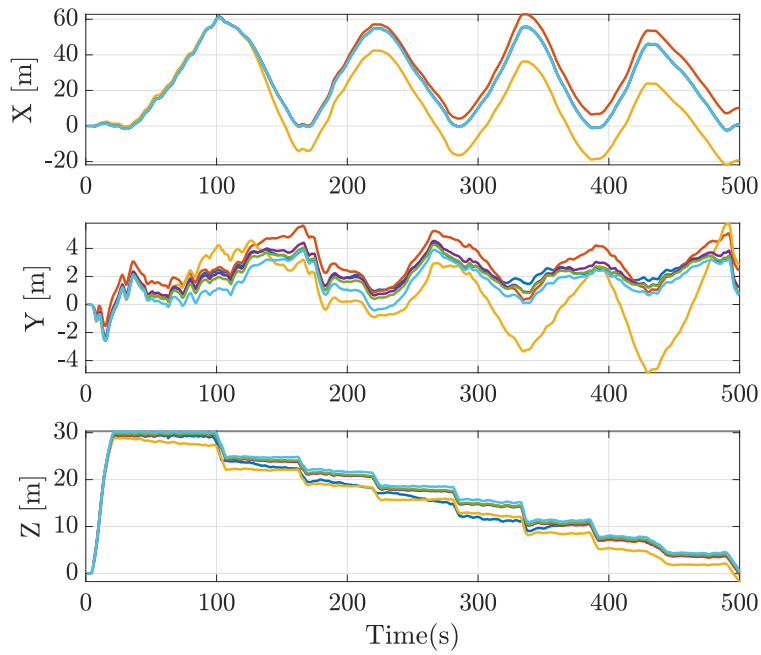


Figure 18: The estimation on X,Y,Z directions.

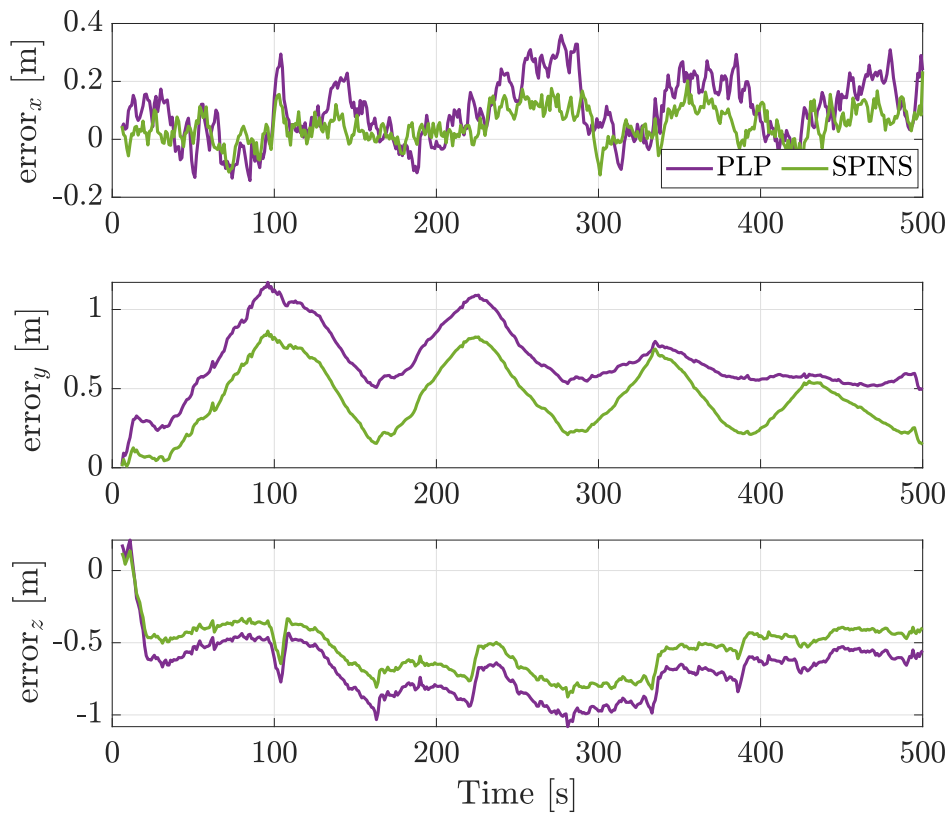


Figure 19: The localization errors on X,Y,Z directions.

where

$$\begin{aligned} \mathbf{H} = & \mathbf{J}_p^T \mathbf{P}_p^{-1} \mathbf{J}_p + \sum_{m \in T_t} \mathbf{J}_m^T \Sigma_m^{-1} \mathbf{J}_m \\ & + \sum_{i \in P_t} \mathbf{J}_i^T \Sigma_i^{-1} \mathbf{J}_i + \sum_{j \in L_t} \mathbf{J}_j^T \Sigma_j^{-1} \mathbf{J}_j + \sum_{k \in \Pi_t} \mathbf{J}_k^T \Sigma_k^{-1} \mathbf{J}_k \\ & + \sum_{s \in S_t} \mathbf{J}_s^T \Sigma_s^{-1} \mathbf{J}_s, \end{aligned}$$

and

$$\begin{aligned} \mathbf{b} = & \mathbf{r}_p^T \mathbf{P}_p^{-1} \mathbf{J}_p^T + \sum_{m \in T_t} \mathbf{r}_m^T \Sigma_m^{-1} \mathbf{J}_m \\ & + \sum_{i \in P_t} \mathbf{r}_i^T \Sigma_i^{-1} \mathbf{J}_i + \sum_{j \in L_t} \mathbf{r}_j^T \Sigma_j^{-1} \mathbf{J}_j + \sum_{k \in \Pi_t} \mathbf{r}_k^T \Sigma_k^{-1} \mathbf{J}_k \\ & + \sum_{s \in S_t} \mathbf{r}_s^T \Sigma_s^{-1} \mathbf{J}_s, \end{aligned}$$

and $\text{const}(\hat{\mathcal{X}})$ is a constant term depending only on $\hat{\mathcal{X}}$.

As a result, (30) can be minimized by solving

$$(\mathbf{H} + \lambda \mathbf{I}) \Delta \mathcal{X} = -\mathbf{b}, \quad (31)$$

where λ is a damping factor. The estimation is hereafter updated as

$$\hat{\mathcal{X}} = \hat{\mathcal{X}} \boxplus \Delta \mathcal{X}. \quad (32)$$

The update iterates until convergence.

B Jacobians of Heterogeneous Feature Measurements

B.1 Point Measurement Jacobians

The Jacobians, based on the formulations in (29), are related to the state of the point in Euclidean space $\mathbf{x}_i = {}^G \mathbf{p}_i$, and the pose of the robot in $\text{SE}(3)$, and can be calculated as follows.

$$\mathbf{J}_{\hat{\mathbf{x}}_i}^{\mathbf{r}_i} = \left. \frac{\partial \mathbf{r}_i(\hat{\mathbf{x}}_i + \Delta \mathbf{x}_i)}{\partial \Delta \mathbf{x}_i} \right|_{\Delta \mathbf{x}_i = \mathbf{0}} = {}^I_G \hat{\mathbf{R}}, \quad (33)$$

and

$$\begin{aligned} \mathbf{J}_{\hat{\mathbf{p}}_I}^{\mathbf{r}_i} &= \left. \frac{\partial \mathbf{r}_i(\hat{\mathbf{x}}_I \boxplus \Delta \mathbf{x}_I)}{\partial \delta \mathbf{p}_I} \right|_{\Delta \mathbf{x}_I = \mathbf{0}} = -{}^I_G \hat{\mathbf{R}}, \\ \mathbf{J}_{\hat{q}_I}^{\mathbf{r}_i} &= \left. \frac{\partial \mathbf{r}_i(\hat{\mathbf{x}}_I \boxplus \Delta \mathbf{x}_I)}{\partial \delta \theta_I} \right|_{\Delta \mathbf{x}_I = \mathbf{0}} = -{}^I_G \hat{\mathbf{R}} [\hat{\mathbf{p}}_i]_{\times}, \end{aligned} \quad (34)$$

where $\Delta \mathbf{x}_i$ and $\Delta \mathbf{x}_I$ are the perturbations on $\hat{\mathbf{x}}_i$ and $\hat{\mathbf{x}}_I$, respectively. Specifically, $[\delta \theta_I^\top, \delta \mathbf{p}_I^\top]^\top$ are the rotational and translational part of the perturbation $\Delta \mathbf{x}_I$. The measurement Jacobians over other parts of \mathbf{x}_I are $\mathbf{0}$.

B.2 Line Measurement Jacobians

The measurement residual Jacobian w.r.t the local pose is

$$\begin{aligned}
\mathbf{J}_{\hat{\mathbf{q}}_I}^{\mathbf{r}_j} &= \left. \frac{\partial \mathbf{r}_j(\hat{\mathbf{x}}_I \boxplus \Delta \mathbf{x}_I)}{\partial \delta \boldsymbol{\theta}_I} \right|_{\Delta \mathbf{x}_I = \mathbf{0}} \\
&= \begin{bmatrix} \left[\begin{array}{c} {}^I_G \hat{\mathbf{R}}^G \hat{\mathbf{n}}_j \\ - \left[{}^I_G \hat{\mathbf{R}} \left[{}^G \hat{\mathbf{p}}_I \right]_{\times} {}^G \hat{\mathbf{v}}_j \end{array} \right]_{\times} \\ - \left[{}^I_G \hat{\mathbf{R}}^G \hat{\mathbf{v}}_j \right]_{\times} \end{bmatrix}, \\
\mathbf{J}_{\hat{\mathbf{p}}_I}^{\mathbf{r}_j} &= \left. \frac{\partial \mathbf{r}_j(\hat{\mathbf{x}}_I \boxplus \Delta \mathbf{x}_I)}{\partial \delta \mathbf{p}_I} \right|_{\Delta \mathbf{x}_I = \mathbf{0}} \\
&= \begin{bmatrix} {}^I_G \hat{\mathbf{R}} \left[{}^G \hat{\mathbf{v}}_j \right]_{\times} \\ \mathbf{0}_3 \end{bmatrix}.
\end{aligned} \tag{35}$$

The measurement residual Jacobians w.r.t. to line state can be calculated using the chain rule as

$$\mathbf{J}_{\hat{\mathbf{x}}_j}^{\mathbf{r}_j} = \mathbf{J}_{\hat{\mathbf{l}}_j}^{\mathbf{r}_j} \mathbf{J}_{\hat{\mathbf{x}}_j}^{\hat{\mathbf{l}}_j}, \tag{36}$$

where $\hat{\mathbf{l}}_j = [\hat{q}_k^\top \ d_j]^\top$ is an intermediate state. Specifically, with perturbation $\delta \hat{\mathbf{l}}_j = [\delta \boldsymbol{\theta}_j^\top \ \delta d_j]^\top$ on manifold $\hat{\mathbf{l}}_j$, we have

$$\begin{aligned}
\mathbf{J}_{\hat{\mathbf{l}}_j}^{\mathbf{r}_j} &= \left. \frac{\partial \mathbf{r}_j(\hat{\mathbf{l}}_j \boxplus \delta \hat{\mathbf{l}}_j)}{\partial \delta \hat{\mathbf{l}}_j} \right|_{\delta \hat{\mathbf{l}}_j = \mathbf{0}} \\
&= \begin{bmatrix} {}^I_G \mathbf{R} & -{}^I_G \mathbf{R} \left[{}^G \mathbf{p}_I \right]_{\times} \\ \mathbf{0}_3 & {}^I_G \mathbf{R} \end{bmatrix} \begin{bmatrix} {}^G \hat{d}_j \left[{}^G \hat{\mathbf{R}}_j \mathbf{e}_1 \right]_{\times} & {}^G \hat{\mathbf{R}}_j \mathbf{e}_1 \\ \left[{}^G \hat{\mathbf{R}}_j \mathbf{e}_2 \right]_{\times} & \mathbf{0}_{3 \times 1} \end{bmatrix},
\end{aligned} \tag{37}$$

and

$$\mathbf{J}_{\hat{\mathbf{x}}_j}^{\hat{\mathbf{l}}_j} = \left. \frac{\partial \hat{\mathbf{l}}_j(\hat{\mathbf{x}}_j + \Delta \mathbf{x}_j)}{\partial \Delta \mathbf{x}_j} \right|_{\Delta \mathbf{x}_j = \mathbf{0}} = \begin{bmatrix} \frac{2}{d} (\hat{q}_j \mathbf{I}_3 - [\hat{\mathbf{q}}_j]_{\times}) & -\frac{2}{q} \hat{\mathbf{q}}_j \\ \hat{\mathbf{q}}_j^\top & \hat{q}_j \end{bmatrix}, \tag{38}$$

where $\mathbf{e}_1, \mathbf{e}_2$ are the first and second column of the identity matrix \mathbf{I}_3 . \mathbf{q}_j and q_j are the vector part and scalar part of the quaternion \hat{q}_j , respectively. Please refer to (Yang and Huang, 2019a) for detailed derivation of (38).

B.3 Plane Measurement Jacobians

By defining an intermediate state of the plane as $\hat{\mathbf{p}}_j = [{}^G \hat{\mathbf{n}}_k^\top \ {}^G d_k]^\top$, the measurement residual \mathbf{r}_k 's Jacobian w.r.t. the plane state $\mathbf{x}_k = {}^G \mathbf{p}_k$ can be calculated using the chain rule as

$$\mathbf{J}_{\hat{\mathbf{x}}_k}^{\mathbf{r}_k} = \mathbf{J}_{\hat{\mathbf{p}}_k}^{\mathbf{r}_k} \mathbf{J}_{\hat{\mathbf{x}}_k}^{\hat{\mathbf{p}}_k}, \tag{39}$$

where

$$\begin{aligned}
\mathbf{J}_{\hat{\mathbf{p}}_k}^{\mathbf{r}_k} &= \left. \frac{\partial \mathbf{r}_k(\hat{\mathbf{p}}_k \boxplus \delta \hat{\mathbf{p}}_k)}{\partial \delta \hat{\mathbf{p}}_k} \right|_{\delta \hat{\mathbf{p}}_k = \mathbf{0}} \\
&= \left[{}^I_G \hat{\mathbf{R}} \left(\left({}^G \hat{d}_k - {}^G \hat{\mathbf{n}}_k^\top {}^G \hat{\mathbf{p}}_I \right) \mathbf{I}_3 - {}^G \hat{\mathbf{n}}_k {}^G \hat{\mathbf{p}}_I^\top \right) \quad {}^I_G \hat{\mathbf{R}}^G \hat{\mathbf{n}}_k \right], \\
\mathbf{J}_{\hat{\mathbf{x}}_k}^{\hat{\mathbf{p}}_k} &= \left. \frac{\partial \hat{\mathbf{p}}_k(\hat{\mathbf{x}}_k + \Delta \mathbf{x}_k)}{\partial \Delta \mathbf{x}_k} \right|_{\Delta \mathbf{x}_k = \mathbf{0}} = \begin{bmatrix} (\mathbf{I}_3 - {}^G \hat{\mathbf{n}}_k {}^G \hat{\mathbf{n}}_k^\top) \\ {}^G \hat{d}_k \\ {}^G \hat{\mathbf{n}}_k \end{bmatrix}.
\end{aligned} \tag{40}$$

$\delta \hat{\mathbf{p}}_k$ and $\Delta \mathbf{x}_k$ are perturbations on $\hat{\mathbf{p}}_k$ and $\hat{\mathbf{x}}_k$, respectively.

By injecting a small perturbation of local pose into (11), we have the measurement Jacobian w.r.t. the pose as follows:

$$\begin{aligned} \mathbf{J}_{\hat{q}_I}^{\mathbf{r}_k} &= \left. \frac{\partial \mathbf{r}_k(\hat{\mathbf{x}}_I \boxplus \Delta \mathbf{x}_I)}{\partial \delta \boldsymbol{\theta}} \right|_{\Delta \mathbf{x}_I = \mathbf{0}} \\ &= \left({}^G \hat{d} - {}^G \hat{\mathbf{n}}_\pi^\top {}^G \hat{\mathbf{P}}_I \right) \left[{}^I \hat{\mathbf{R}}^G \hat{\mathbf{n}}_\pi \right]_\times, \end{aligned} \quad (41)$$

$$\mathbf{J}_{\hat{\mathbf{p}}_I}^{\mathbf{r}_k} = \left. \frac{\partial \mathbf{r}_k(\hat{\mathbf{x}}_I \boxplus \Delta \mathbf{x}_I)}{\partial \delta \mathbf{p}_I} \right|_{\Delta \mathbf{x}_I = \mathbf{0}} = -{}^I \hat{\mathbf{R}}^G \hat{\mathbf{n}}_\pi \hat{\mathbf{n}}_\pi^\top. \quad (42)$$

C Jacobians of the Structural Priors Measurements

C.1 Point-Point Measurement Jacobians

For a pair of points $(i, i') \in \mathcal{S}$, the Jacobians of the measurement residual, defined as $\mathbf{r} = \mathbf{z} - h_{ii'}(\hat{\mathbf{x}}_i, \hat{\mathbf{x}}_{i'})$, are derived as

$$\mathbf{J}_{\hat{\mathbf{x}}_i}^{\mathbf{r}_{ii'}} = \mathbf{J}_{\hat{\mathbf{x}}_{i'}}^{\mathbf{r}_{ii'}} \mathbf{J}_{\hat{\mathbf{x}}_i}^{\hat{\mathbf{x}}_{i'}}, \quad (43)$$

$$\mathbf{J}_{\hat{\mathbf{x}}_{i'}}^{\mathbf{r}_{ii'}} = \mathbf{J}_{\hat{\mathbf{x}}_{i'}}^{\mathbf{r}_{ii'}} \mathbf{J}_{\hat{\mathbf{x}}_{i'}}^{\hat{\mathbf{x}}_{i'}}, \quad (44)$$

where $\mathbf{J}_{\hat{\mathbf{x}}_i}^{\hat{\mathbf{x}}_{i'}} = -\mathbf{I}_3$, $\mathbf{J}_{\hat{\mathbf{x}}_{i'}}^{\hat{\mathbf{x}}_{i'}} \mathbf{J}_{\hat{\mathbf{x}}_{i'}}^{\hat{\mathbf{x}}_{i'}} = \mathbf{I}_3$.

Specifically, if we consider $h_{ii'}(\cdot)$ as a distance measurement function, the Jacobians can be calculated as

$$\mathbf{J}_{\hat{\mathbf{x}}_{i'}}^{\mathbf{r}_{ii'}} = \frac{\hat{\mathbf{x}}_{ii'}}{\|\hat{\mathbf{x}}_{ii'}\|}. \quad (45)$$

C.2 Point-Line Measurement Jacobians

The measurement residual Jacobian with respect to the point i is

$$\mathbf{J}_{\hat{\mathbf{x}}_i}^{\mathbf{r}_{ij}} = \mathbf{J}_{\hat{\mathbf{p}}_{ij}}^{\mathbf{r}_{ij}} \mathbf{J}_{\hat{\mathbf{x}}_i}^{\mathbf{p}_{ij}}, \quad (46)$$

where $\mathbf{J}_{\hat{\mathbf{x}}_i}^{\mathbf{p}_{ij}} = \begin{bmatrix} \hat{\mathbf{n}}_j^\top \\ \hat{\mathbf{n}}_j^\top \times \hat{\mathbf{v}}_j^\top \end{bmatrix}$.

The measurement residual Jacobian with respect to the line estimation error is

$$\mathbf{J}_{\hat{\mathbf{p}}_j}^{\mathbf{r}_{ij}} = \mathbf{J}_{\hat{\mathbf{p}}_{ij}}^{\mathbf{r}_{ij}} \mathbf{J}_{\hat{\mathbf{l}}_j}^{\mathbf{p}_{ij}} \mathbf{J}_{\hat{\mathbf{p}}_j}^{\hat{\mathbf{l}}_j}, \quad (47)$$

where

$$\mathbf{J}_{\hat{\mathbf{l}}_j}^{\mathbf{p}_{ij}} = \begin{bmatrix} {}^G \hat{\mathbf{p}}_i [\hat{\mathbf{R}}_j \mathbf{e}_1]_\times & {}^G \hat{\mathbf{p}}_i \hat{\mathbf{R}}_j \mathbf{e}_1 \\ {}^G \hat{\mathbf{p}}_i [\hat{\mathbf{R}}_j \mathbf{e}_3]_\times & 1 \end{bmatrix},$$

and $\mathbf{J}_{\hat{\mathbf{p}}_j}^{\hat{\mathbf{l}}_j}$ is calculated in (38). When considering the measurement as point-line distance, $\mathbf{J}_{\hat{\mathbf{p}}_{ij}}^{\mathbf{r}_{ij}} = \frac{\hat{\mathbf{p}}_{ij}}{\|\hat{\mathbf{p}}_{ij}\|}$.

C.3 Point-Plane Measurement Jacobians

The measurement residual Jacobian with respect to the point estimate error is

$$\mathbf{J}_{\hat{\mathbf{x}}_i}^{\mathbf{r}_{ij}} = {}^G \hat{\mathbf{n}}_k^\top. \quad (48)$$

The measurement residual Jacobian with respect to the plane estimate error is

$$\mathbf{J}_{\hat{\mathbf{x}}_k}^{\mathbf{r}^{ij}} = \mathbf{J}_{\hat{\mathbf{p}}_k}^{\mathbf{r}^{ij}} \mathbf{J}_{\hat{\mathbf{x}}_k}^{\hat{\mathbf{p}}^{ij}}, \quad (49)$$

where

$$\mathbf{J}_{\hat{\mathbf{p}}_k}^{\mathbf{r}^{ij}} = [G \hat{\mathbf{p}}_i^\top \quad 1]^\top,$$

and $\mathbf{J}_{\hat{\mathbf{x}}_k}^{\hat{\mathbf{p}}^{ij}}$ is provided in (40).

C.4 Line-Line Measurement Jacobians

The Jacobians of the measurement error $\alpha_{jj'}$ and $d_{jj'}$ w.r.t. the estimation error are

$$\mathbf{J}_{\hat{\mathbf{x}}_j}^{\mathbf{r}^{\alpha_{jj'}}} = \mathbf{J}_{\hat{\mathbf{l}}_j}^{\mathbf{r}^{\alpha_{jj'}}} \mathbf{J}_{\hat{\mathbf{x}}_j}^{\hat{\mathbf{l}}_j}, \quad (50)$$

where

$$\mathbf{J}_{\hat{\mathbf{l}}_j}^{\mathbf{r}^{\alpha_{jj'}}} = \hat{\mathbf{v}}_{j'}^\top [[\hat{\mathbf{R}}_j \mathbf{e}_2]_\times \quad \mathbf{0}_{3 \times 1}].$$

The measurement residual Jacobian w.r.t. j' can be calculated similarly. Specifically, when two lines are parallel, namely $\bar{\mathbf{v}}_j = \pm \bar{\mathbf{v}}_{j'}$, the distance measurement Jacobian can be calculated as

$$\mathbf{J}_{\hat{\mathbf{x}}_j}^{\mathbf{r}^{d_{jj'}}} = \mathbf{J}_{\hat{\mathbf{l}}_j}^{\mathbf{r}^{d_{jj'}}} \mathbf{J}_{\hat{\mathbf{x}}_j}^{\hat{\mathbf{l}}_j}, \quad (51)$$

where

$$\mathbf{J}_{\hat{\mathbf{l}}_j}^{\mathbf{r}^{d_{jj'}}} = \hat{\mathbf{v}}_{j'} \times [d_j [\hat{\mathbf{R}}_j \mathbf{e}_1]_\times \quad \hat{\mathbf{R}}_j \mathbf{e}_1]. \quad (52)$$

C.5 Line-Plane Measurement Jacobians

The directional correlation measurement Jacobian is as follows

$$\mathbf{J}_{\hat{\mathbf{x}}_j}^{\mathbf{r}^{\alpha_k}} = \mathbf{J}_{\hat{\mathbf{l}}_j}^{\mathbf{r}^{\alpha_k}} \mathbf{J}_{\hat{\mathbf{x}}_j}^{\hat{\mathbf{l}}_j}, \quad (53)$$

where

$$\mathbf{J}_{\hat{\mathbf{l}}_j}^{\mathbf{r}^{\alpha_k}} = [[\hat{\mathbf{R}}_j \mathbf{e}_3]_\times \quad \mathbf{0}_{3 \times 1}], \quad (54)$$

and

$$\mathbf{J}_{\hat{\mathbf{x}}_k}^{\mathbf{r}^{\alpha_k}} = \frac{\hat{\mathbf{v}}_j^\top (\mathbf{I}_3 - G \hat{\mathbf{n}}_k \hat{\mathbf{n}}_k^\top)}{G \hat{d}_k}. \quad (55)$$

When the line j is parallel to the plane, namely $\bar{\mathbf{v}}_j^\top \mathbf{n}_k = 0$, the distance residual Jacobians

$$\mathbf{J}_{\hat{\mathbf{x}}_j}^{\mathbf{r}^{d_k}} = \mathbf{J}_{\hat{\mathbf{l}}_j}^{\mathbf{r}^{d_k}} \mathbf{J}_{\hat{\mathbf{x}}_j}^{\hat{\mathbf{l}}_j}, \quad (56)$$

where

$$\mathbf{J}_{\hat{\mathbf{l}}_j}^{\mathbf{r}^{d_k}} = \hat{\mathbf{n}}_k^\top [[\hat{\mathbf{R}}_j \mathbf{e}_2]_\times \quad \hat{\mathbf{R}}_j \mathbf{e}_2], \quad (57)$$

and

$$\mathbf{J}_{\hat{\mathbf{x}}_k}^{\mathbf{r}^{d_k}} = \frac{(\hat{\mathbf{n}}_j \times \hat{\mathbf{v}}_j)^\top (\mathbf{I}_3 - G \hat{\mathbf{n}}_k \hat{\mathbf{n}}_k^\top) G \hat{d}_j}{G \hat{d}_k} + G \hat{\mathbf{n}}_k^\top. \quad (58)$$

C.6 Plane-Plane Measurement Jacobians

The Jacobian of the angle measurement residual is

$$\mathbf{J}_{\hat{\mathbf{x}}_k}^{\alpha_{kk'}} = \frac{(\hat{\mathbf{n}}_{k'})^\top (\mathbf{I}_3 - {}^G\hat{\mathbf{n}}_k^G \hat{\mathbf{n}}_k^\top)}{{}^G\hat{d}_k}. \quad (59)$$

The distance measurement residual is calculated as

$$\mathbf{J}_{\hat{\mathbf{x}}_k}^d = \frac{{}^G\hat{\mathbf{p}}_k - {}^G\hat{\mathbf{p}}_{k'}}{\|{}^G\hat{\mathbf{p}}_k - {}^G\hat{\mathbf{p}}_{k'}\|} \quad (60)$$

The Jacobian w.r.t. the plane k' can be calculated similarly.

Acknowledgments

The work is supported by National Research Foundation (NRF) Singapore, ST Engineering-NTU Corporate Lab under its NRF Corporate Lab@ University Scheme.

References

- Aloise, I., Corte, B. D., Nardi, F., and Grisetti, G. (2019). Systematic Handling of Heterogeneous Geometric Primitives in Graph-SLAM Optimization. *IEEE Robotics and Automation Letters*, 4(3):2738–2745.
- Burri, M., Nikolic, J., Gohl, P., Schneider, T., Rehder, J., Omari, S., Achtelik, M. W., and Siegwart, R. (2016). The EuRoC Micro Aerial Vehicle Datasets. *The International Journal of Robotics Research*, 35(10):1157–1163.
- Caballero, F. and Merino, L. (2021). Dll: Direct Lidar Localization. A Map-based Localization Approach for Aerial Robots. In *2021 IEEE/RSJ International Conference on Intelligent Robots and Systems (IROS)*, pages 5491–5498. IEEE.
- Cai, G., Dias, J., and Seneviratne, L. (2014). A Survey of Small-scale Unmanned Aerial Vehicles: Recent Advances and Future Development Trends. *Unmanned Systems*, 2(02):175–199.
- Carlone, L. and Karaman, S. (2019). Attention and Anticipation in Fast Visual-Inertial Navigation. *IEEE Transactions on Robotics*, 35(1):1–20.
- Chavez, A., L’Heureux, D., Prabhakar, N., Clark, M., Law, W.-L., and Prazenica, R. J. (2017). Homography-based State Estimation for Autonomous Uav Landing. In *AIAA Information Systems-AIAA Infotech Aerospace*. American Institute of Aeronautics and Astronautics.
- Dellaert, F. (2012). Factor Graphs and GTSAM: A Hands-on Introduction. Technical report, Georgia Institute of Technology.
- Durrant-Whyte, H. and Bailey, T. (2006). Simultaneous Localization and Mapping: Part i. *IEEE Robotics & Automation Magazine*, 13(2):99–110.
- Forster, C., Carlone, L., Dellaert, F., and Scaramuzza, D. (2017). On-manifold Preintegration for Real-Time Visual-Inertial Odometry. *IEEE Transactions on Robotics*, 33(1):1–21.
- Fu, Q., Wang, J., Yu, H., Ali, I., Guo, F., and Zhang, H. (2020). PL-VINS: Real-Time Monocular Visual-Inertial SLAM with Point and Line. *arXiv e-prints*, pages arXiv–2009.
- Geneva, P., Eckenhoff, K., Yang, Y., and Huang, G. (2018). LIPS: Lidar-Inertial 3D Plane SLAM. In *2018 IEEE/RSJ International Conference on Intelligent Robots and Systems (IROS)*, pages 123–130. IEEE.

- Gomez-Ojeda, R., Moreno, F.-A., Zuñiga-Noël, D., Scaramuzza, D., and Gonzalez-Jimenez, J. (2019). PL-SLAM: A Stereo SLAM System Through the Combination of Points and Line Segments. *IEEE Transactions on Robotics*, 35(3):734–746.
- Hasan, A., Qadir, A., Nordeng, I., and Neubert, J. (2017). Aided Inertial Navigation: Unified Feature Representations and Observability Analysis. In *Proceedings of the International Symposium on Automation and Robotics in Construction (ISARC)*, pages 1–8. IAARC.
- He, Y., Zhao, J., Guo, Y., He, W., and Yuan, K. (2018). PL-VIO: Tightly-Coupled Monocular Visual-Inertial Odometry Using Point and Line Features. *Sensors*, 18(4):1159.
- Hodge, W. V. D., Hodge, W., and Pedoe, D. (1994). *Methods of Algebraic Geometry: Volume 1*, volume 2. Cambridge University Press.
- Huber, P. J. (1992). Robust Estimation of A Location Parameter. In *Breakthroughs in statistics*, pages 492–518. Springer.
- Jovančević, I., Viana, I., Orteu, J.-J., Sentenac, T., and Larnier, S. (2016). Matching CAD Model and Image Features for Robot Navigation and Inspection of an Aircraft. In *Proceedings of the 5th International Conference on Pattern Recognition Applications and Methods*, page 359–366. SCITEPRESS - Science and Technology Publications, Lda.
- Kaess, M., Johannsson, H., Roberts, R., Ila, V., Leonard, J. J., and Dellaert, F. (2012). iSAM2: Incremental Smoothing and Mapping Using the Bayes Tree. *The International Journal of Robotics Research*, 31(2):216–235.
- Kottas, D. G. and Roumeliotis, S. I. (2013). Efficient and Consistent Vision-aided Inertial Navigation using Line Observations. In *2013 IEEE International Conference on Robotics and Automation*, pages 1540–1547. IEEE.
- Lemaire, T., Berger, C., Jung, I.-K., and Lacroix, S. (2007). Vision-based SLAM: Stereo and Monocular Approaches. *International Journal of Computer Vision*, 74(3):343–364.
- Li, X., He, Y., Lin, J., and Liu, X. (2020). Leveraging Planar Regularities for Point Line Visual-Inertial Odometry. *arXiv preprint arXiv:2004.11969*.
- Lu, Y. and Song, D. (2015). Robust rgb-d odometry using point and line features. In *The IEEE International Conference on Computer Vision (ICCV)*.
- Lyu, Y., Yuan, S., and Xie, L. (2022). Structure Priors aided Visual-Inertial Navigation in Building Inspection Tasks with Auxiliary Line Features. *IEEE Transactions on Aerospace and Electronic Systems*, pages 1–1.
- Middelberg, S., Sattler, T., Untzelmann, O., and Kobbelt, L. (2014). Scalable 6-DOF Localization on Mobile Devices. In *European conference on computer vision*, pages 268–283. Springer.
- Mühlfellner, P., Bürki, M., Bosse, M., Derendarz, W., Philippsen, R., and Furgale, P. (2016). Summary Maps for Lifelong Visual Localization. *Journal of Field Robotics*, 33(5):561–590.
- Mur-Artal, R., Montiel, J. M. M., and Tardós, J. D. (2015). ORB-SLAM: A Versatile and Accurate Monocular SLAM System. *IEEE Transactions on Robotics*, 31(5):1147–1163.
- Mur-Artal, R. and Tardós, J. D. (2017). Visual-Inertial Monocular SLAM with Map Reuse. *IEEE Robotics and Automation Letters*, 2(2):796–803.
- Nardi, F., Corte, B. D., and Grisetti, G. (2019). Unified Representation and Registration of Heterogeneous Sets of Geometric Primitives. *IEEE Robotics and Automation Letters*, 4(2):625–632.
- Nguyen, T.-M., Cao, M., Yuan, S., Lyu, Y., Nguyen, T. H., and Xie, L. (2021a). LIRO: Tightly Coupled Lidar-Inertia-Ranging Odometry. In *2021 IEEE International Conference on Robotics and Automation (ICRA)*, pages 14484–14490.

- Nguyen, T.-M., Yuan, S., Cao, M., Lyu, Y., Nguyen, T. H., and Xie, L. (2021b). NTU VIRAL: A Visual-Inertial-Ranging-Lidar Dataset, from An Aerial Vehicle Viewpoint. *The International Journal of Robotics Research*, page 02783649211052312.
- Padhy, R. P., Xia, F., Choudhury, S. K., Sa, P. K., and Bakshi, S. (2019). Monocular vision aided autonomous uav navigation in indoor corridor environments. *IEEE Transactions on Sustainable Computing*, 4(1):96–108.
- Platinsky, L., Szabados, M., Hlasek, F., Hemsley, R., Del Pero, L., Pancik, A., Baum, B., Grimmett, H., and Ondruska, P. (2020). Collaborative Augmented Reality on Smartphones via Life-long City-scale Maps. *ISMAR*.
- Pumarola, A., Vakhitov, A., Agudo, A., Sanfeliu, A., and Moreno-Noguer, F. (2017). PL-SLAM: Real-time Monocular Visual SLAM with Points and Lines. In *2017 IEEE international conference on robotics and automation (ICRA)*, pages 4503–4508. IEEE.
- Qin, T., Cao, S., Pan, J., and Shen, S. (2019). A General Optimization-based Framework for Global Pose Estimation with Multiple Sensors. *arXiv preprint arXiv:1901.03642*.
- Qin, T., Li, P., and Shen, S. (2018). Vins-mono: A Robust and Versatile Monocular Visual-Inertial State Estimator. *IEEE Transactions on Robotics*, 34(4):1004–1020.
- Sattler, T., Leibe, B., and Kobbelt, L. (2011). Fast image-based localization using direct 2d-to-3d matching. In *2011 International Conference on Computer Vision*, pages 667–674. IEEE.
- Sattler, T., Maddern, W., Toft, C., Torii, A., Hammarstrand, L., Stenborg, E., Safari, D., Okutomi, M., Pollefeys, M., Sivic, J., et al. (2018). Benchmarking 6DOF Outdoor Visual Localization in Changing Conditions. In *Proceedings of the IEEE Conference on Computer Vision and Pattern Recognition*, pages 8601–8610.
- Shamaiah, M., Banerjee, S., and Vikalo, H. (2010). Greedy Sensor Selection: Leveraging Submodularity. In *49th IEEE conference on decision and control (CDC)*, pages 2572–2577. IEEE.
- Shan, T., Englot, B., Ratti, C., and Rus, D. (2021). LVI-SAM: D-coupled Lidar-Visual-Inertial Odometry via Smoothing and Mapping. *arXiv preprint arXiv:2104.10831*.
- Strasdat, H., Montiel, J., and Davison, A. J. (2010). Scale Drift-aware Large Scale Monocular SLAM. *Robotics: Science and Systems VI*, 2(3):7.
- Sturm, J., Engelhard, N., Endres, F., Burgard, W., and Cremers, D. (2012). A Benchmark for the Evaluation of RGB-D SLAM systems. In *2012 IEEE/RSJ International Conference on Intelligent Robots and Systems*, pages 573–580. IEEE.
- Weiss, S., Scaramuzza, D., and Siegwart, R. (2011). Monocular-slam-based navigation for autonomous micro helicopters in gps-denied environments. *Journal of Field Robotics*, 28(6):854–874.
- Yang, Y., Geneva, P., Eckenhoff, K., and Huang, G. (2019). Visual-Inertial Odometry with Point and Line Features. In *2019 IEEE/RSJ International Conference on Intelligent Robots and Systems (IROS)*, pages 2447–2454.
- Yang, Y., Geneva, P., Zuo, X., Eckenhoff, K., Liu, Y., and Huang, G. (2019). Tightly-coupled Aided Inertial Navigation with Point and Plane Features. In *2019 International Conference on Robotics and Automation (ICRA)*, pages 6094–6100. IEEE.
- Yang, Y. and Huang, G. (2019a). Aided Inertial Navigation: Unified Feature Representations and Observability Analysis. In *2019 International Conference on Robotics and Automation (ICRA)*, pages 3528–3534. IEEE.
- Yang, Y. and Huang, G. (2019b). Observability Analysis of Aided INS With Heterogeneous Features of Points, Lines, and Planes. *IEEE Transactions on Robotics*, 35(6):1399–1418.

- Yuan, S., Wang, H., and Xie, L. (2021). Survey on Localization Systems and Algorithms for Unmanned Systems. *Unmanned Systems*, 9(02):129–163.
- Zhang, J. and Singh, S. (2014). LOAM: Lidar Odometry and Mapping in Real-time. In *Robotics: Science and Systems*, volume 2.
- Zhang, J. and Singh, S. (2015). Visual–Inertial Combined Odometry System for Aerial Vehicles. *Journal of Field Robotics*, 32(8):1043–1055.
- Zhang, J., Zeng, G., and Zha, H. (2019). Structure-Sware SLAM With Planes and Lines in Man-made Environment. *Pattern Recognition Letters*, 127:181–190.
- Zhang, Z. and Scaramuzza, D. (2018). A Tutorial on Quantitative Trajectory Evaluation for Visual(-Inertial) Odometry. In *IEEE/RSJ Int. Conf. Intell. Robot. Syst. (IROS)*.
- Zheng, F., Tsai, G., Zhang, Z., Liu, S., Chu, C.-C., and Hu, H. (2018). Trifo-VIO: Robust and Efficient Stereo Visual Inertial Odometry using Points and Lines. In *2018 IEEE/RSJ International Conference on Intelligent Robots and Systems (IROS)*, pages 3686–3693. IEEE.
- Zuo, X., Ye, W., Yang, Y., Zheng, R., Vidal-Calleja, T., Huang, G., and Liu, Y. (2020). Multimodal Localization: Stereo over LiDAR Map. *Journal of Field Robotics*, 37(6):1003–1026.